The Journal of Physiology

The upregulation of K^+ and HCN channels in developing spiral ganglion neurons is mediated by cochlear inner hair cells

Linus J. Conrad[1], Fiorella C. Grandi[2], Adam J. Carlton[1], Jing-Yi Jeng[1], Lara de Tomasi[1], Patryk Zarecki[1], Walter Marcotti[1,3], Stuart L. Johnson[1,3] and Mirna Mustapha[1,3]

[1]*School of Biosciences, University of Sheffield, Sheffield, UK*
[2]*INSERM, Institute de Myologie, Centre de Recherche en Myologie F-75013, Sorbonne Université, Paris, France*
[3]*Neuroscience Institute, University of Sheffield, Sheffield, UK*

Handling Editors: Nathan Schoppa & Conny Kopp-Scheinpflug

The peer review history is available in the Supporting Information section of this article (https://doi.org/10.1113/JP286134#support-information-section).

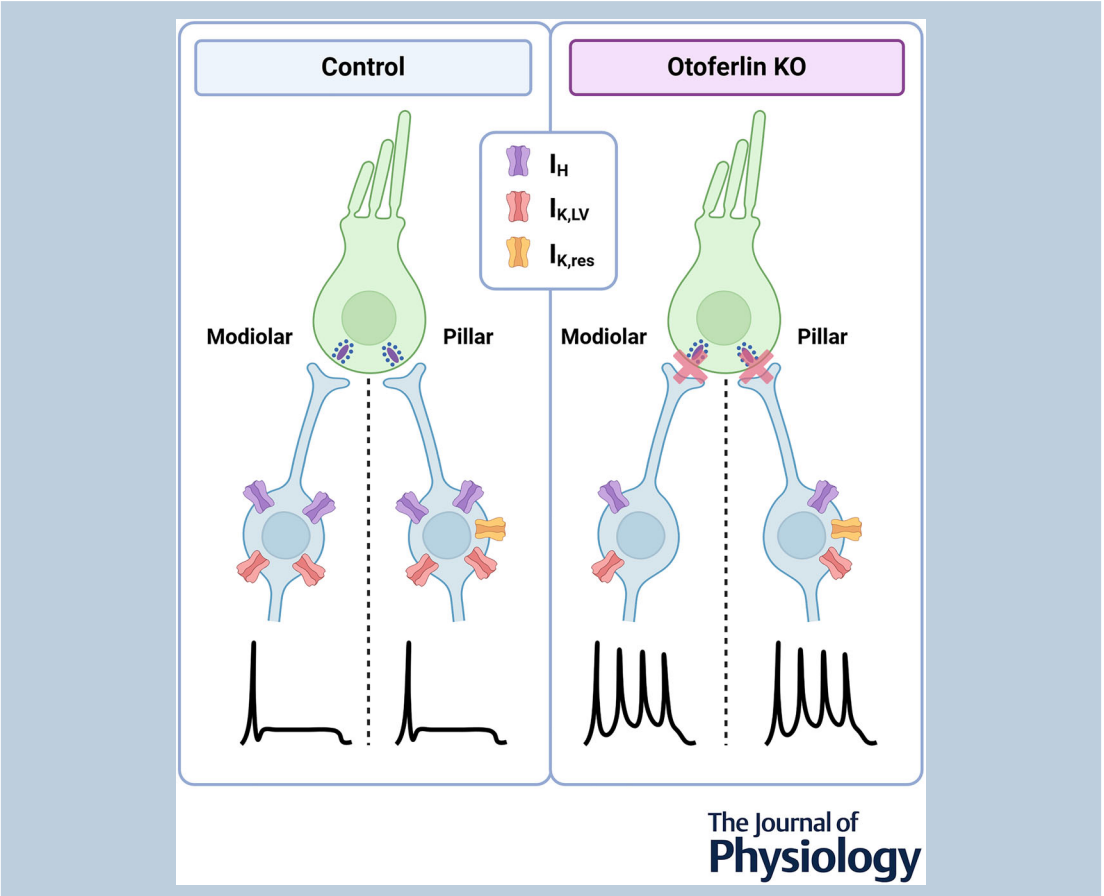

Abstract figure legend We investigated the progressive changes in the biophysical properties of the spiral ganglion neurons (SGNs, shown in light blue) of the mouse cochlea. In the absence of otoferlin, which is the primary Ca^{2+} sensor for neurotransmitter release in the inner hair cells (IHCs, shown in green), SGNs in the pre-hearing cochlea fail to upregulate basolateral membrane channels resulting in their hyperexcitability. The functional maturation of SGNs depends on spontaneous release of glutamate from developing IHCs.

DOI: 10.1113/JP286134

Abstract Spiral ganglion neurons (SGNs) are primary sensory afferent neurons that relay acoustic information from the cochlear inner hair cells (IHCs) to the brainstem. The response properties of different SGNs diverge to represent a wide range of sound intensities in an action-potential code. This biophysical heterogeneity is established during pre-hearing stages of development, a time when IHCs fire spontaneous Ca^{2+} action potentials that drive glutamate release from their ribbon synapses onto the SGN terminals. The role of spontaneous IHC activity in the refinement of SGN characteristics is still largely unknown. Using pre-hearing *otoferlin* knockout mice (*Otof*$^{-/-}$), in which Ca^{2+}-dependent exocytosis in IHCs is abolished, we found that developing SGNs fail to upregulate low-voltage-activated K^+-channels and hyperpolarisation-activated cyclic-nucleotide-gated channels. This delayed maturation resulted in hyperexcitable SGNs with immature firing characteristics. We have also shown that SGNs that synapse with the pillar side of the IHCs selectively express a resurgent K^+ current, highlighting a novel biophysical marker for these neurons. RNA-sequencing showed that several K^+ channels are downregulated in *Otof*$^{-/-}$ mice, further supporting the electrophysiological recordings. Our data demonstrate that spontaneous Ca^{2+}-dependent activity in pre-hearing IHCs regulates some of the key biophysical and molecular features of the developing SGNs.

(Received 14 December 2023; accepted after revision 2 September 2024; first published online 23 September 2024)
Corresponding authors M. Mustapha and S. Johnson: School of Biosciences, University of Sheffield, Sheffield, UK. Email: mirna.m@sheffield.ac.uk; s.johnson@sheffield.ac.uk

Key points

- Ca^{2+}-dependent exocytosis in inner hair cells (IHCs) is otoferlin-dependent as early as postnatal day 1.
- A lack of otoferlin in IHCs affects potassium channel expression in SGNs.
- The absence of otoferlin is associated with SGN hyperexcitability.
- We propose that type I spiral ganglion neuron functional maturation depends on IHC exocytosis.

Introduction

Populations of neurons can display a surprising level of heterogeneity between individual cells and can often be grouped into different neuronal subtypes based on defining criteria such as connectivity, gene expression, and morphological and biophysical properties (Mukamel & Ngai, 2019; Zeng & Sanes, 2017). During development, pre-determined genetic programmes and their modulation by patterns of spontaneous network activity combine to determine the identity of neurons (Turrigiano & Nelson, 2004; West & Greenberg, 2011). This is particularly important in peripheral sensory systems, such as the retina and inner ear, which undergo a significant period of refinement prior to being able to respond to external stimuli (Pumo et al., 2022). In the mature cochlea, acoustic information is transformed into an action potential code at ribbon synapses between inner hair cells (IHCs) and type-I spiral ganglion neurons (SGNs). A mature SGN terminal forms only one synapse with an adult IHC (Pujol et al., 1998), with up to around 20 SGNs contacting a single IHC in mice (Meyer et al., 2009). SGNs on the same IHC show segregation around the IHC basolateral membrane according to their threshold for sound detection and firing rate. In the cat, *in vivo* recordings have shown that low-threshold SGN

Linus Conrad received his BSc in Biomedical Science at the University of Cambridge (UK). He was a Research Associate in the Hearing Research Group at the University of Sheffield (https://www.sheffield.ac.uk/hearing) between 2020 and 2023. His research investigates changes in the biophysical and morphological properties of spiral ganglion neurons in the mammalian cochlea, with the overall aim of furthering our understanding of the mechanisms involved in cochlear development.

fibres, with a high spontaneous rate, preferentially contact the pillar side of IHCs (towards the outer hair cells), whereas high-threshold fibres, with a low spontaneous rate, primarily contact the modiolar side (towards the central axis of the cochlea) (Heil & Peterson, 2015; Liberman, 1978; Liberman et al., 1990). The diversity in the physiological properties of SGNs is likely to be required to convey the wide dynamic range of sound intensity encoded by each IHC (Winter et al., 1990).

The intrinsic biophysical properties of type I SGNs have been extensively studied using *in vitro* preparations, which have revealed key molecular players regulating their excitability. Whole-cell patch-clamp recordings from cultured SGNs have established three distinct firing patterns in response to current injection (Crozier & Davis, 2014; Davis & Crozier, 2015), which correspond to the three canonical classes of action-potential initiation (Prescott et al., 2008). Tonic firing and slowly adapting responses (class 1) have been recorded in SGNs that have a high input resistance, slow membrane responses and predominantly express high-voltage-activated K^+ currents. Single-firing and unitary adapting neurons (class 3) are characterised by a low-input resistance, rapid membrane responses and large low-voltage-activated K^+ currents. Phasic firing and rapidly adapting (class 2) neurons present an intermediate phenotype. Recent studies using single-cell RNA sequencing have also highlighted the presence of three SGN subtypes based on a unique combination of molecular markers such as Ca^{2+} binding proteins, guidance molecules and ion channels (Grandi et al., 2020; Petitpré et al., 2018; Shrestha et al., 2018; Sun et al., 2018). Although the possible presence of these three distinct SGN subclasses is not obvious from recent electrophysiological measurements (Siebalda et al., 2023), their molecular identity is primarily defined during pre-hearing stages of development (Grandi et al., 2020; Petitpré et al., 2020; Petitpré et al., 2022; Sanders & Kelley, 2022; Sun et al., 2018; Shrestha et al., 2018; Siebald et al., 2023). In the pre-hearing cochlea, immature IHCs exhibit intrinsic Ca^{2+} action potentials that are modulated by spontaneous Ca^{2+} waves propagating within the sensory epithelium through supporting cells (Eckrich et al., 2018; Johnson et al., 2011, 2017; Tritsch et al., 2007; Wang et al., 2015). This Ca^{2+}-dependent activity in the IHCs is relayed onto type I SGNs via specialised ribbon synapses, resulting in the characteristic bursting firing pattern observed in the immature afferent fibres (Jones et al., 2007) and the central auditory pathway (Babola et al., 2018; Sonntag et al., 2009). Genetic ablation of the glutamate transporter VGlut3 in the IHCs has been shown to disrupt the burst-like firing pattern of the developing SGNs and leads to their death (Babola et al., 2018; Shrestha et al., 2018; Sun et al., 2018).

In this study, we used the otoferlin mutant ($Otof^{-/-}$) mouse model of congenital deafness in which Ca^{2+}-dependent exocytosis is almost completely abolished (Roux et al., 2006) to study whether the acquisition of type I SGN biophysical diversity was affected by the loss of input from the IHCs. We found that the absence of otoferlin was associated with SGN hyperexcitability, which was caused by the failure of SGNs to up-regulate low-voltage-activated K^+ currents and hyperpolarisation-activated cyclic-nucleotide-gated (HCN) ion channels. We also found that a resurgent K^+ current was selectively expressed in type I SGNs forming axo-somatic terminals with the pillar side of the IHCs. These physiological observations might be explained by the differential expression of number of potassium channels revealed by RNAseq in $Otof^{-/-}$ mice. However, we did not find any correlation between the input resistance of SGNs and their position around the basolateral membrane of the IHCs, as previously reported in rats (Markowitz & Kalluri, 2020).

Methods

Ethical statement

Animal work was licensed by the Home Office under the Animals (Scientific Procedures) Act 1986 (PPL_PCC8E5E93 and PP1481074) and was approved by the University of Sheffield Ethical Review Committee (180 626_Mar). Mice were killed by cervical dislocation followed by decapitation. Mice had free access to food and water and a 12 h light–dark cycle. *Otoferlin* heterozygous ($Otof^{+/-}$) and knockout ($Otof^{-/-}$) mice (Roux et al., 2006) were bred with a mouse line expressing *Ai14*-tdTomato in the spiral ganglion neurons (*Bhlb5-Cre X Ai14*-tdTomato; Grandi et al., 2020). Littermate mice of either sex were used for experiments.

Sample preparation for SGN electrophysiological measurements

The cochlea from mice between postnatal day 2 (P2) and P8, where the day of birth corresponds to P0, was removed from the skull and immediately transferred into ice-cold dissection solution (in mM): 220 sucrose, 5.8 KCl, 1.3 $CaCl_2$, 0.9 $MgCl_2$, 10 HEPES, 5.6 glucose, 0.7 NaH_2PO_4, 2 kynueric acid, 2 sodium pyruvate, amino acids and vitamins, which were added from concentrates (Thermo Fisher Scientific, Cambridge, UK). The pH was adjusted to 7.48 with NaOH. The apical coil of the cochlea, which included the SGNs, was transferred to a customised recording chamber (e.g. Carlton et al., 2023, 2024). The tissue was then digested for 4–8 min under shaking and at 37°C with 1 mg/ml collagenase dispase (cat. no. 10269638001, Roche, Welwyn Garden City, UK) dissolved in the above solution. The digestion process was terminated by adding fetal bovine serum (diluted

1:2 using the dissection solution) in ice-cold extracellular solution. The chamber containing the cochleae immersed in the recording extracellular solution (see below) was then transferred to the electrophysiological set-up for electrophysiological recordings.

SGN electrophysiological recordings

SGNs were patch-clamped *in situ* using a semi-intact preparation as previously described (Markowitz et al., 2022). Patch clamp recordings were performed using an Axopatch 200B amplifier and a Digidata 1550B (Molecular Devices, San Jose, CA, USA). Data were acquired at a 50 kHz sampling rate and were low-pass filtered with a 5 kHz cut-off (Axopatch on-board filter). Patch pipettes were prepared from soda-lime glass and coated with surf-wax (Mr Zoggs SexWax, Carpinteria, CA, USA) up to the tip to reduce stray capacitance. Pipette resistance ranged from 2.8 to 3.5 MΩ. Pipette solution contained (in mM): 28 KMeSo4, 90 KCl, 0.1 $CaCl_2$, 4 $MgCl_2$, 5 EGTA, 4 Na_2ATP, 0.3 NaGTP, 10 sodium phosphocreatine and 2 mg/ml biocytin (cat. no. B4261, Sigma/Merck, Gillingham, UK). The extracellular solution used for the recordings contained (in mM): 135 NaCl, 5.8 KCl, 1.3 $CaCl_2$, 0.9 $MgCl_2$, 10 HEPES, 5.6 glucose, 0.7 NaH_2PO_4, 2 sodium pyruvate supplemented with vitamins and amino acids. The junction potential was empirically determined to be 4.8 mV and subtracted from the command potential (for voltage clamp) or from the voltage traces (for current clamp). To allow the patch pipette to reach the spiral ganglion neuron soma, the satellite glia cells were removed using a pressurised cleaning pipette mounted on a micromanipulator. Whole-cell recordings were obtained from superficial neurons on the scala tympani surface of the ganglion, which proved the most accessible. Capacitance and series resistance were compensated using the Axopatch 200B circuitry. Series resistance (R_s) compensation was set to 95% prediction with compensation of >80%. The residual uncompensated R_s was typically 6−8 MΩ and recordings with R_s >12 MΩ were excluded from analysis. SGNs were investigated using different command protocols, which allowed the measurements of their biophysical characteristics. Since SGNs show a wide range of input resistance during development, current-clamp protocols with different stimulation strengths were used to avoid response saturation.

The contribution of different K^+ channels expressed in the SGNs was investigated by applying specific K^+ channel blockers as previously shown (Johnston et al., 2010). Blockers were applied cumulatively as follows: TTX (1 µM, cat. no. 1069: Tocris, Bristol, UK), DtX-α or DtX-I (100 nM, cat. no. 74504-53-3 and cat. no. 107950-33-4, respectively, Alomone Labs, Jerusalem, Israel), tetraethyl ammoniumchloride (TEA, 1 mM, cat. no. 86614, Sigma/Merck) and 4-amino-pyridine (4-AP, 5 mM, cat. no. 275875, Sigma/Merck). In addition, the pipette solution contained 10 µM ZD7288 (cat. no. 133059-99-1, Tocris) to block HCN channels.

Electrophysiological raw data were semi-automatically processed using custom-written software in R and python based on the pyabf API to read Axopatch binary files. In brief, the software allowed action potential detection and the extraction of key features based on the amplitude and rate of change (first derivative) of the voltage time-series data. The 'tidyverse' paradigm functions were used to reshape and process the data (Wickham et al., 2019). The code is freely available within the R-package (wctools) on github.

The capacitative transients were fitted using a biexponential decay: $I_{norm} = A_1 \exp(-t/\tau_1) + A_2 \exp(-t/\tau_2)$, where A_1 and A_2 represent the amplitude at the start of the voltage-pulse and τ_1 and τ_2 are the fast and slow time constants of the decay, respectively. The decay time constant of the K^+ currents were fitted by an asymptotic decay function: $I = A + (R_0 - A)\exp(-t/\tau)$, where A is the asymptote, and R_0 the value at $t = 0$ and τ the time constant of decay. The sigmoid distribution of voltage-dependent gating responses was fitted with a Boltzmann function: $g_{norm} = 1/(1 + \exp((V - V_h)/k))$, where V_h is the half-activation voltage (determining centre of the transition) and k the slope factor (determining steepness of the transition). All models were optimised with a Levenberg–Marquardt algorithm as implemented in the R package minpack.lm (Elzhov et al., 2022).

SGN fibre tracing

Following the whole-cell electrophysiological recordings, the pipette was retracted from the SGNs, which in more than half of the cases resulted in an outside-out patch (resistance >400 MΩ), leaving the neuron soma intact. Then, the tissue was transferred into a 4% paraformaldehyde in phosphate-buffered solution for 20 min at room temperature. All following steps were done as described in the 'Immunostaining' section below. The IHCs were labelled using the rabbit-IgG anti-MYO7a primary antibodies (1:500, cat. no. 25-6790: Proteus Biosciences, Ramona, CA, USA). The next day, samples were stained in a with a goat-anti-rabbit secondary antibody conjugated with Alexa405 (1:400 dilution, cat. no. A-31556, Thermo Fisher Scientific) and a streptavidin-Alexa647 conjugate (1:1000 dilution, cat. no. S-21374, Thermo Fisher Scientific). Samples were then mounted onto slides and sealed with Vectashield (Vector Laboratories, Burlingame, CA, USA). Imaging data for fibre tracing were acquired using a Nikon W1 spinning disk confocal microscope (Wolfson light microscopy

facility, University of Sheffield, UK). The position of the traced fibre on the base of the IHCs was quantified as normalised basal position (NBP) as previously described (Markowitz & Kalluri, 2020).

Basolateral membrane current and capacitance recordings in IHCs

The mouse cochlea was dissected and kept in the following extracellular solution (in mM): 135 NaCl, 5.8 KCl, 1.3 $CaCl_2$, 0.9 $MgCl_2$, 0.7 NaH_2PO_4, 5.6 D-glucose, 10 Hepes–NaOH. Sodium pyruvate (2 mM), MEM amino acids solution (50×, without L-glutamine) and MEM vitamins solution (100×) were added from concentrates (Thermo Fisher Scientific). The pH was adjusted to 7.48 with NaOH (osmolality ∼308 mOsm kg^{-1}). Once dissected, the cochleae were transferred to a microscope chamber and immobilised under a nylon mesh attached to a stainless-steel ring. The organs of Corti were viewed with an upright microscope (Nikon FN-1, Nikon, Minato City/Tokyo, Japan) with Nomarski differential interference contrast (DIC) optics. IHC recordings were performed using an Optopatch amplifier (Cairn Research Ltd, Faversham, UK) with cells maintained in the above extracellular solution and at body temperature (35–37°C). Patch pipettes were pulled from soda glass capillaries with a typical resistance in extracellular solution of 2–3 MΩ. Patch electrodes were coated with surf wax (Mr Zoggs SexWax) to reduce the electrode capacitance. Data acquisition was controlled by pClamp software using a Digidata 1550B (Molecular Devices). Recordings were stored on a computer for off-line analysis (Clampfit, Molecular Devices; Origin 2024: OriginLab Corp., Northampton, MA, USA). Action potentials in IHCs were recorded using the following intracellular solution (in mM): 131 KCl, 3 $MgCl_2$, 1 EGTA–KOH, 5 Na_2ATP, 5 HEPES–KOH, 10 sodium phosphocreatine (pH was adjusted with 1 M KOH to 7.28; 294 mOsm kg^{-1}). Real-time changes in membrane capacitance (ΔC_m) were measured using the Optopatch amplifier as previously described (Johnson et al., 2017). Briefly, a 4 kHz sine wave of 13 mV root mean square was applied to IHCs from the membrane potential of −81 mV and was interrupted for the duration of the voltage step. The capacitance signal was filtered at 250 Hz and sampled at 5 kHz. ΔC_m was measured by averaging the C_m trace over a 200 ms period following the voltage step and subtracting the pre-pulse baseline. Data were acquired using pClamp software and a Digidata 1550B and analysed with Origin (OriginLab). Membrane potentials were corrected for the voltage drop across R_s and a liquid junction potential of −11 mV, measured between electrode and bath solutions. Capacitance measurement experiments were performed in the extracellular presence of 30 mM TEA, 15 mM 4-AP and 300 nM apamin (cat. no. 1652, Tocris) to block the K^+ currents and allow for the analysis of calcium currents (I_{Ca}) during the voltage step. The intracellular solution for these experiments was (in mM): 110 caesium glutamate, 20 $CsCl_2$, 3 $MgCl_2$, 1 EGTA–CsOH, 5 Na_2ATP, 5 HEPES–KOH, 10 sodium phosphocreatine, 0.3 GTP (pH was adjusted with 1 M CsOH to 7.28; 294 mOsm kg^{-1}). The liquid junction potential was −11 mV for this intracellular solution.

Immunofluorescence

The inner ear was immersed in 4% paraformaldehyde in phosphate-buffered saline (PBS, pH 7.4) for 20 min at room temperature and then washed three times in PBS for 10 min. The apical coil of the organ of Corti was then washed in PBS, removed by fine dissection, and incubated in PBS supplemented with 5% normal goat or horse serum and 0.5% Triton X-100 for 1 h at room temperature. The samples were immunolabelled with primary antibodies overnight at 37°C, washed three times with PBS and incubated with the secondary antibodies for 1 h at 37°C. Antibodies were prepared in 1% serum and 0.5% Triton X-100 in PBS. Primary antibodies were: mouse IgG1 anti-CtBP2 (1:200, cat. no. 612044, Biosciences, UK); rabbit-IgG anti-MYO7a (1:500, cat. no. 25-6790, Proteus BD Biosciences, MIlpitas, CA); anti-tubulin beta 3 mouse-IgG2a (1:1000, cat. no. 801201, BioLegend, San Diego, CA, USA). Secondary antibodies were species-appropriate Alexa Fluor or Northern Lights secondary antibodies. Samples were mounted in Vectashield (H-1000). The images from the apical cochlear region (8–12 kHz) were captured with a Zeiss LSM 880 AiryScan equipped with Plan-Apochromat ×63 oil DIC M27 objective (Wolfson light microscopy facility). The number of synaptic ribbon (CtBP2) puncta was calculated from the z-stack images of the immunolabelled proteins using Imaris (Oxford Instruments, Abingdon, UK). Individual puncta were assigned to two separate groups (pillar or modiolar) using *k*-means clustering (a method of clustering each observation with the nearest mean: McQueen, 1967) of their position along the pillar to modiolar axis with $k = 2$ clusters. Individual IHCs were manually identified, and every protein punctum was automatically assigned to one IHC based on its centroid position.

RNA isolation and library preparation for RNA-sequencing

The sensory epithelium and spiral ganglion neurons were micro-dissected in DNase free ice-cold PBS 1× and immediately snap frozen in liquid nitrogen. Each batch of P7 was the result of pooling tissue from three

to four mice of each genotype; two pools of tissue were sequenced for each genotype. RNA was extracted using RNeasy Plus Micro Kit (Qiagen, Hilden, Germany) according to manufacturer's instructions. RNA quantity was established using a NanoDrop spectrophotometer (Thermo Fisher Sceintific) and RNA integrity number (RIN) was calculating using a BioAnalyzer. All samples had RIN score greater than 9.1. mRNA library preparation was performed using poly A enrichment and sequenced on the Illumina NovaSeq sequencer (Illumina, San Diego, CA, USA) using paired-end 150 bp reads.

RNA-sequencing analysis and differential gene expression

The sequencing libraries were processed using the nf-core RNA pipeline (Ewels et al., 2020, https://nf-co.re/rnaseq/usage) using the standard parameters. Reads were mapped to the mouse genome (mm10). The resulting gene counts were determined using Salmon (Patro et al., 2017) and used for downstream analysis with DeSeq2 (Love et al., 2014). Metascape (Zhou et al., 2019) and Reactome (Gillespie et al., 2022) were used to query for enriched GO and pathways in the list of differentially expressed genes. RPM (reads per million) bigwig files were created using R using the packages Rsamtools (Morgan et al., 2023), rtracklayer (Lawrence et al., 2009), and Genomic Ranges (Lawrence et al., 2013) and were visualised using the Washington University Genome browser (http://epigenomegateway.wustl.edu/).

RNAscope

RNA gene expression was performed as previously described (Grandi et al., 2020) using RNAscope Multiplex Fluorescent Reagent Kit v2 Assay (ACD-Bio, ∼323,270). Inner ear tissue from P6 mice was dissected in ice-cold PBS and placed in 4% paraformaldehyde at 4°C for 24 h with gentle shaking. Samples were then washed 3× with ice-cold PBS and gradually embedded with 10%, 20% and 30% sucrose at 4°C for >24 h, which was followed by the embedding of the tissue in OCT. The OCT-embedded tissue was sectioned (14 µm thick) using a cryostat and collected on the SuperFrost Plus Adhesion slides (Epredia, Leicestershire, 10149870). The manufacturer-designed RNAscope probes used for labelling were Mm-Kcnip3-C1 (ACD-Bio, abingdon, cat. no. 561321-C1) and Mm-Cacna1a-C2 (ACD-Bio, cat. no. 493141-C2). The fluorophores used for imaging were TSA Vivid Fluorophore Kit 520 (Tocris Bioscience, cat. no. 7523) and TSA Vivid Fluorophore Kit 570 (Tocris Bioscience, cat. no. 7526). A Zeiss LSM 980 Airyscan 2 microscope (Zeiss Microscopy, Jena, Germany) was used for imaging and z-stack images were captured at 0.150 µm intervals. The images were then processed using Fiji ImageJ and the fluorescence intensity was quantified by measuring the raw integrated density of the projected images.

Statistical analysis

Statistical comparisons of means were made using Student's unpaired two-tailed *t* test, pair-wise comparisons of means using the Tukey's HSD (honestly significant difference) test, the Wilcoxon test, one-way ANOVA or a linear regression model. For the latter, the *P* values testing for the difference in means (main effect) and difference in rate of maturation (interaction effect) were adjusted with the false discovery rate (FDR) method. $P < 0.05$ was selected as the criterion for statistical significance. Average values are quoted in text and figures as means ± SD. Animals of either sex were randomly assigned to the different experimental groups. No statistical methods were used to define sample size, which was determined based on previously published similar work from our laboratory. Animals were taken from several cages and breeding pairs over a period of several months.

Results

Exocytosis is abolished in IHCs from newborn otoferlin-deficient (*Otof*$^{-/-}$) mice

To determine whether the input from developing IHCs is required for the acquisition of the biophysical characteristics of mature SGNs, we used a constitutive knockout mouse for otoferlin (*Otof*$^{-/-}$). Otoferlin is the major Ca^{2+} sensor for vesicle fusion in cochlear IHCs (Roux et al., 2006). However, otoferlin has been shown to be required for IHC exocytosis only from P4 onwards with an otoferlin-independent mechanism present at earlier stages (Beurg et al., 2010). Therefore, we first investigated whether IHC ribbon synapses showed normal exocytosis prior to P4. IHC synaptic function was estimated by measuring the size of the Ca^{2+} current (I_{Ca}) and the induced change in cell membrane capacitance (ΔC_m) following depolarising voltage steps. We found that exocytosis in P2 *Otof*$^{-/-}$ mice was nearly abolished despite having a comparable I_{Ca} size to littermate control *Otof*$^{+/-}$ mice (Fig. 1*A*–*E*). The rate of neurotransmitter release in P2–P3 IHCs was investigated by determining ΔC_m in response to depolarisations to −11 mV of varying duration (2 ms to 1.0 s; interstep interval was at least 11 s), which reveals the emptying of different populations of synaptic vesicle pools (Fig. 1*C* and *D*). When using a physiological extracellular Ca^{2+} concentration (1.3 mM Ca^{2+}) and body temperature, stimuli up to about 50 ms

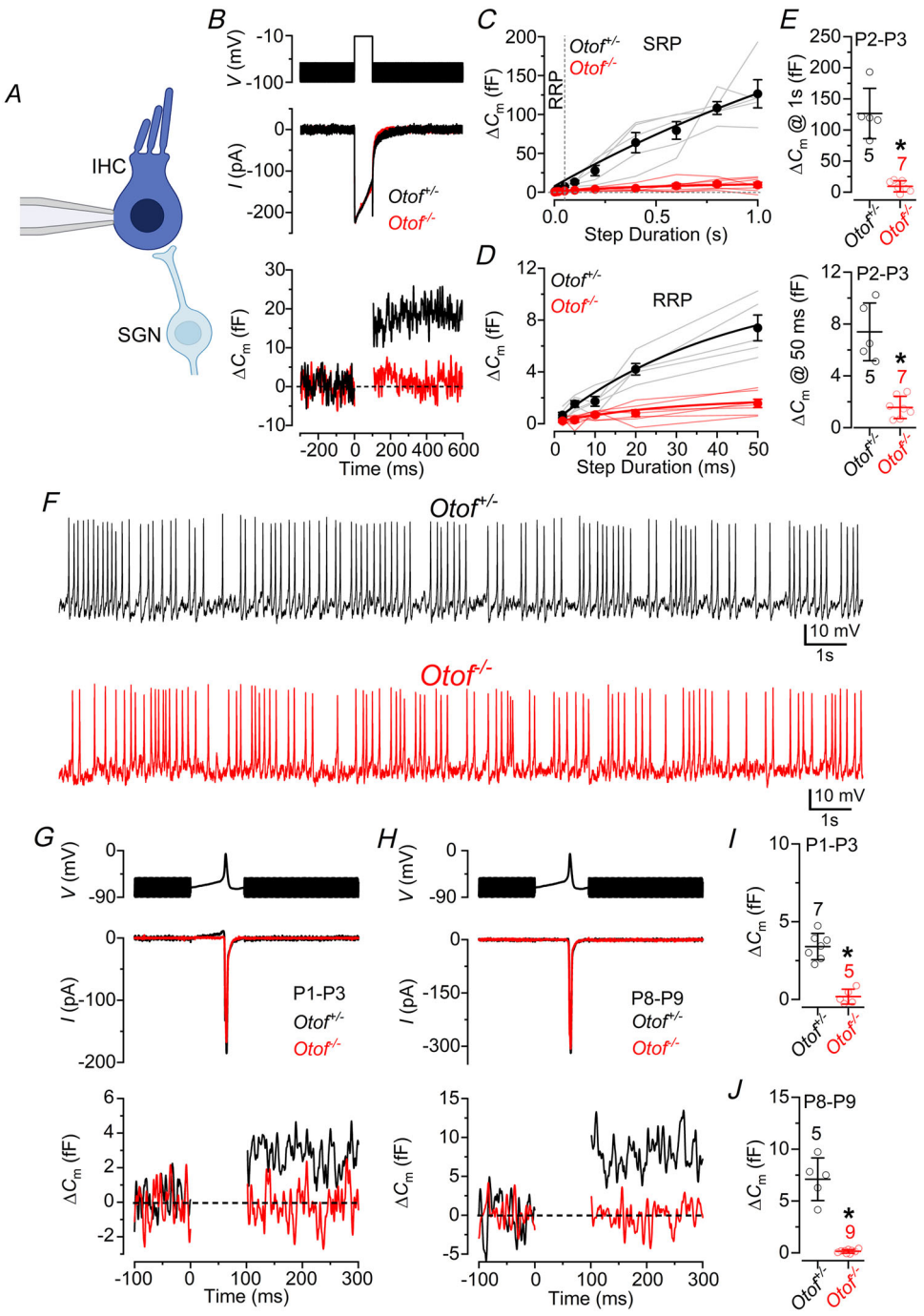

Figure 1. Calcium-dependent exocytosis is abolished in IHCs from P2 *Otof*$^{-/-}$ mice
A, cartoon showing the patch pipette attached to the cell body of an IHC, which forms a synapse with the bouton-like axon terminal of a spiral ganglion neuron (SGN). *B*, calcium current (I_{Ca}: middle panel) and corresponding change in membrane capacitance (ΔC_m: bottom panel) recorded from apical coil IHCs of P2 control *Otof*$^{+/-}$ (black) and knockout *Otof*$^{-/-}$ (red) mice. Recordings were obtained in response to a 100 ms voltage step from the holding potential of −81 mV to −11 mV (top panel). *C*, average ΔC_m recorded from IHCs of 5 *Otof*$^{+/-}$ and 7 *Otof*$^{-/-}$ IHCs (P2–P3) in response to voltage steps from 2 ms to 1.0 s (to −11 mV from the holding of −81 mV) showing the readily releasable pool (RRP: 2 ms to 50 ms) and the secondary releasable pool (SRP: 100 ms to 1.0 s). *D*, expanded view of the RRP (from 2 ms to 50 ms) from *C*. *E*, size of the total vesicle releasable pool measured in the P2–P3 IHCs at 1 s (RRP + SRP, top panel) and that of the isolated RRP at 50 ms (lower panel). Both RRP and SRP were significantly reduced in the IHCs of *Otof*$^{-/-}$ (5 IHCs from 3 mice) compared to those in control *Otof*$^{+/-}$ (7 IHCs from 3 mice) mice. *F*, typical example of spontaneous action potentials recorded from P5 IHCs of *Otof*$^{+/-}$ (top panel) and *Otof*$^{-/-}$ (bottom panel) mice. *G* and *H*, I_{Ca} (middle panel) and corresponding ΔC_m (bottom panel) recorded from *Otof*$^{+/-}$ and *Otof*$^{-/-}$ newborn (*G*) and pre-hearing (*H*) mice in response to

an action potential voltage protocol (instead of voltage steps as done for *B–E*). *I* and *J*, size of ΔC_m measured in response to the action potential protocol in IHCs from both genotypes at P1–P3 (*I*: *Otof*$^{+/-}$: 7 IHCs from 3 mice; *Otof*$^{-/-}$: 5 IHCs from 2 mice) and P8–P9 (*J*: *Otof*$^{+/-}$: 5 IHCs from 3 mice; *Otof*$^{-/-}$: 9 IHCs from 3 mice). Data in *C–E*, *I* and *J* are plotted as means ± SD.

reveal the readily releasable pool (RRP), while longer steps cause the release of vesicles located further away from the Ca^{2+} channels (secondarily releasable pool: SRP) (Johnson et al., 2010, 2017). The total releasable vesicle pools (RRP + SRP) and the isolated RRP were almost completely abolished in IHCs from P2–P3 *Otof*$^{-/-}$ mice (Fig. 1*E*, $P < 0.0001$ for both RRP + SRP and the isolated RRP comparisons between *Otof*$^{+/-}$ and *Otof*$^{-/-}$ mice, two-way ANOVA).

Having established that in IHCs exocytosis is already dependent on otoferlin in newborn mice, we investigated whether their ability to generate spontaneous Ca^{2+}-dependent action potentials was affected in *Otof*$^{-/-}$ mice (Johnson et al. 2011; Marcotti et al., 2003). We found that all IHCs investigated exhibited spontaneous action potentials at P4–P5 (Fig. 1*E* and *F*), the frequency of which was not significantly different between Otof$^{+/-}$ (3.9 ± 2.4 Hz, 7 IHCs, 3 mice) and *Otof*$^{-/-}$ mice (4.0 ± 3.0 Hz, 7 IHCs, 3 mice, $P = 0.9669$ *t* test). Moreover, the resting membrane potential of IHCs was indistinguishable between *Otof*$^{+/-}$ (−58 ± 3 mV, 7 IHCs, 3 mice) and *Otof*$^{-/-}$ mice (−58 ± 2 mV, 6 IHCs, 3 mice, $P = 0.8467$). Since action potentials are the characteristic physiological response of pre-hearing IHCs, we investigated whether the underlying Ca^{2+} influx during a single action potential was sufficient to trigger exocytosis in newborn (P1–P3: Fig. 1*G* and *I*) and pre-hearing (P8–P9: Fig. 1*H* and *J*) mice. At both age ranges, exocytosis was present in IHCs from *Otof*$^{+/-}$ but almost absent in *Otof*$^{-/-}$ mice ($P < 0.0001$ for both comparisons, one-way ANOVA, Tukey's test).

Altogether, the above results indicate that otoferlin is the Ca^{2+} sensor for exocytosis in IHCs from as early as P1. Despite the nearly abolished exocytosis, pre-hearing IHCs from *Otof*$^{-/-}$ mice exhibited normal biophysical characteristics.

Spiral ganglion neuron maturation is delayed in pre-hearing *Otof*$^{-/-}$ mice

Whole cell patch-clamp recordings were performed on 86 spiral ganglion neurons (SGNs) from *ex vivo* preparations of the mouse cochlea (Fig. 2*A*). Whole-cell SGN recordings were performed with a biocytin-containing intracellular solution, which allowed us to visualise the position of the SGN afferent terminals on the IHCs in 66% of all SGN recordings. Of these recordings, 13% were identified as being from type II SGNs, which were discarded from the following investigation. We cannot exclude that a few recordings from the untraced SGNs could be from type II SGNs, although these are likely to be fewer than five based on their known abundance in the mouse cochlea (about 10%; Ryugo, 1992).

Current injections into SGNs of control *Otof*$^{+/-}$ mice elicited either a single action potential (AP) at the stimulus onset (single), a few APs at the beginning of the stimulus (phasic), or repetitive APs for the entire duration of the stimulus (tonic) (Fig. 2*B*). The proportion of SGNs showing the three different firing patterns changed during development, such that by the end of the first postnatal week only single and phasic SGNs were present in control *Otof*$^{+/-}$ mice (Fig. 2*C*), which is consistent with previous findings (Adamson et al., 2002; Crozier & Davis, 2014; Markowitz & Kalluri, 2020). By contrast, SGNs from *Otof*$^{-/-}$ mice retained all three firing profiles up to at least P8, although the proportion of fibres showing the tonic AP profile was smaller at older ages (Fig. 2*C*). The resting membrane potential (V_m) of the SGNs became progressively more hyperpolarised during postnatal development in both *Otof*$^{+/-}$ and *Otof*$^{-/-}$ mice, although with a significantly smaller rate in the latter (Fig. 2*D*, linear model interaction, $P = 0.0039$). We also found that the resting membrane conductance (g_m) of the SGN measured at the V_m increased during development in both genotypes but was consistently smaller in *Otof*$^{-/-}$ compared to *Otof*$^{+/-}$ mice (Fig. 2*E*, $P < 0.0001$). A similar effect of the genotype was observed for the threshold current injection level required to elicit APs in SGNs, being consistently lower in *Otof*$^{-/-}$ mice (Fig. 2*F*, $P = 0.0432$). Overall, these results indicate that the absence of otoferlin-dependent exocytosis from IHCs causes a delay in the normal maturation of the SGN biophysical properties.

The absence of otoferlin does not affect the number of ribbons nor distribution of SGNs onto the IHCs

We next investigated whether the different firing pattern observed in the SGNs of *Otof*$^{-/-}$ compared to *Otof*$^{+/-}$ mice was correlated with the loss of a specific SGN sub-population contacting the IHCs (Petitpré et al., 2018; Shrestha et al., 2018; Sun et al., 2018). Recent studies in rats have shown that SGNs contacting the modiolar side of IHCs mature faster and are less excitable than neurons on the pillar side (Markowitz & Kalluri, 2020). Therefore, we hypothesised that an absence, or reduced number, of modiolar SGN terminals on IHCs in *Otof*$^{-/-}$ mice could explain why the SGNs in these mice tended

to be slowly maturing and more excitable. To investigate whether the lack of otoferlin had any effect on the ribbon synapses, we performed immunostaining against CtBP2, which is a component of the pre-synaptic machinery, from pre-hearing (P8–P9) and mature (P20) IHC (Fig. 3*A*–*H*). Published work has shown that the number of ribbon synapses is highly reduced in the IHCs from 4-week-old *Otof*$^{-/-}$ mice, but not at P10–P14 (Al-Moyed et al., 2019; Stalmann et al., 2021). However, other studies reported that ribbon number is already highly reduced (about 30–50%) at P15–P17 (Tertrais et al., 2019; Vincent et al., 2017). Our data show that the total number of CtBP2 puncta per IHC was not significantly different between *Otof*$^{+/-}$ and *Otof*$^{-/-}$ mice at both P9 and P20 (Fig. 3*B* and *F*). The numbers of CtBP2 puncta were also similar between the two genotypes when they were separated according to their location on the modiolar or pillar side of the IHCs (P8: Fig. 3*B*; P20: Fig. 3*F*). Interestingly, a previous transmission electron microscopy study showed that although the total number of ribbons was comparable in the IHCs of P15 control and *Otof*$^{-/-}$ mice, the total number of functional synapses, which are defined as synapses with an anchored ribbon, was highly reduced in the latter (Roux et al., 2006). Indeed, we found that despite the similar number of ribbon puncta, the number of SGN afferent fibres approaching the IHCs, quantified

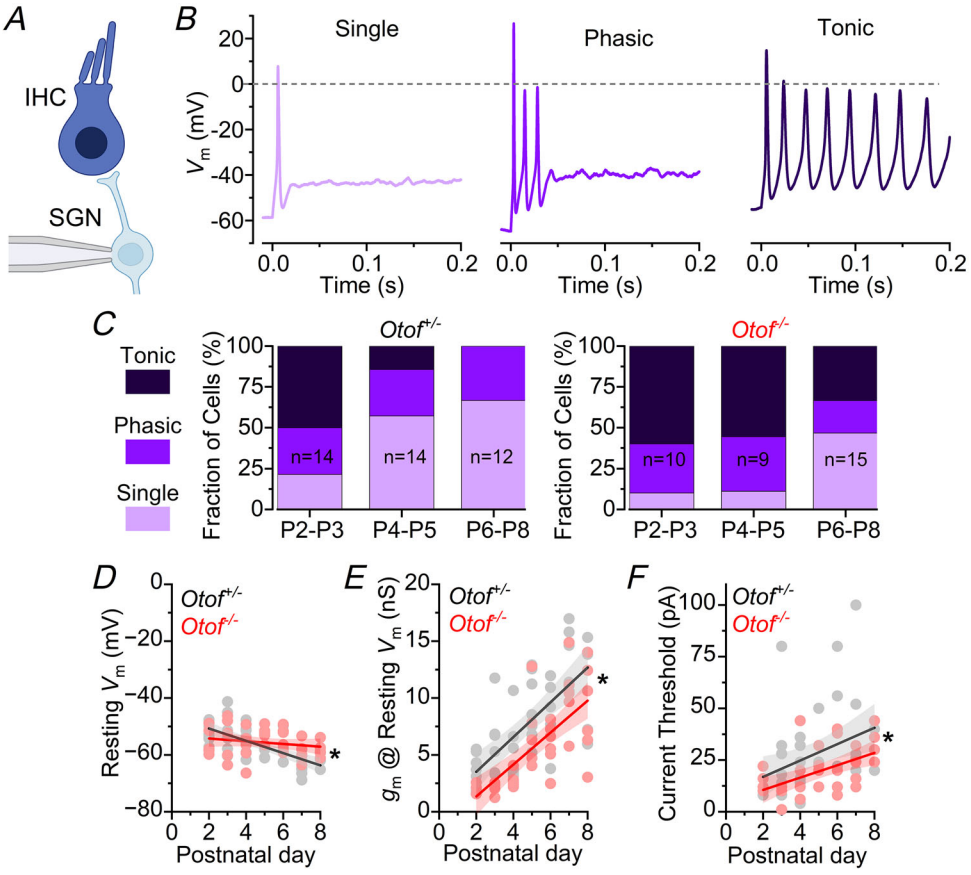

Figure 2. SGN development is delayed in *Otof*$^{-/-}$ mice
A, cartoon showing the patch pipette attached to the cell body of a SGN. *B*, example of SGN recordings showing the three different action potential firing patterns (single, phasic and tonic) from P3 control *Otof*$^{+/-}$ mice. The voltage responses in current clamp were measured by applying 50 pA current injections. *C*, percentage of SGNs exhibiting the different firing patterns at three different age ranges between P2 and P8 from *Otof*$^{+/-}$ (left) and *Otof*$^{-/-}$ (right) mice. Number of SGNs tested at each age group is shown within the columns. *D*–*F*, resting membrane potential (V_m, *D*), resting membrane conductance (g_m, *E*) and the size of the current threshold level required to elicit action potentials (*F*) from SGNs at different postnatal ages from *Otof*$^{+/-}$ and *Otof*$^{-/-}$ mice. V_m was defined as the steady-state membrane potential at rest. The rate of V_m decrease was significantly different between SGNs of *Otof*$^{+/-}$ and *Otof*$^{-/-}$ mice (−2.16 ± 0.36 mV/day *vs*. −0.48± 0.38 mV/day, respectively, 78% decrease, $P = 0.0039$). g_m was defined by the slope of linear response to small negative current injections from V_m, and the rate of change was significantly larger in *Otof*$^{+/-}$ (7.89 ± 0.45 nS) than *Otof*$^{-/-}$ mice (5.37 ± 0.49 nS, 31% decrease, $P < 0.0001$). The rate of current threshold increase was also significantly different between *Otof*$^{+/-}$ (28 ± 2 pA) and *Otof*$^{-/-}$ mice (19 ± 3 pA, 32% decrease, $P = 0.0432$). Number of mice at the different ages from the left to the right in *D*–*F* are: *Otof*$^{+/-}$ 7, 9, 8, 7, 5, 6, 4; *Otof*$^{-/-}$ 5, 7, 4, 5, 6, 6, 6.

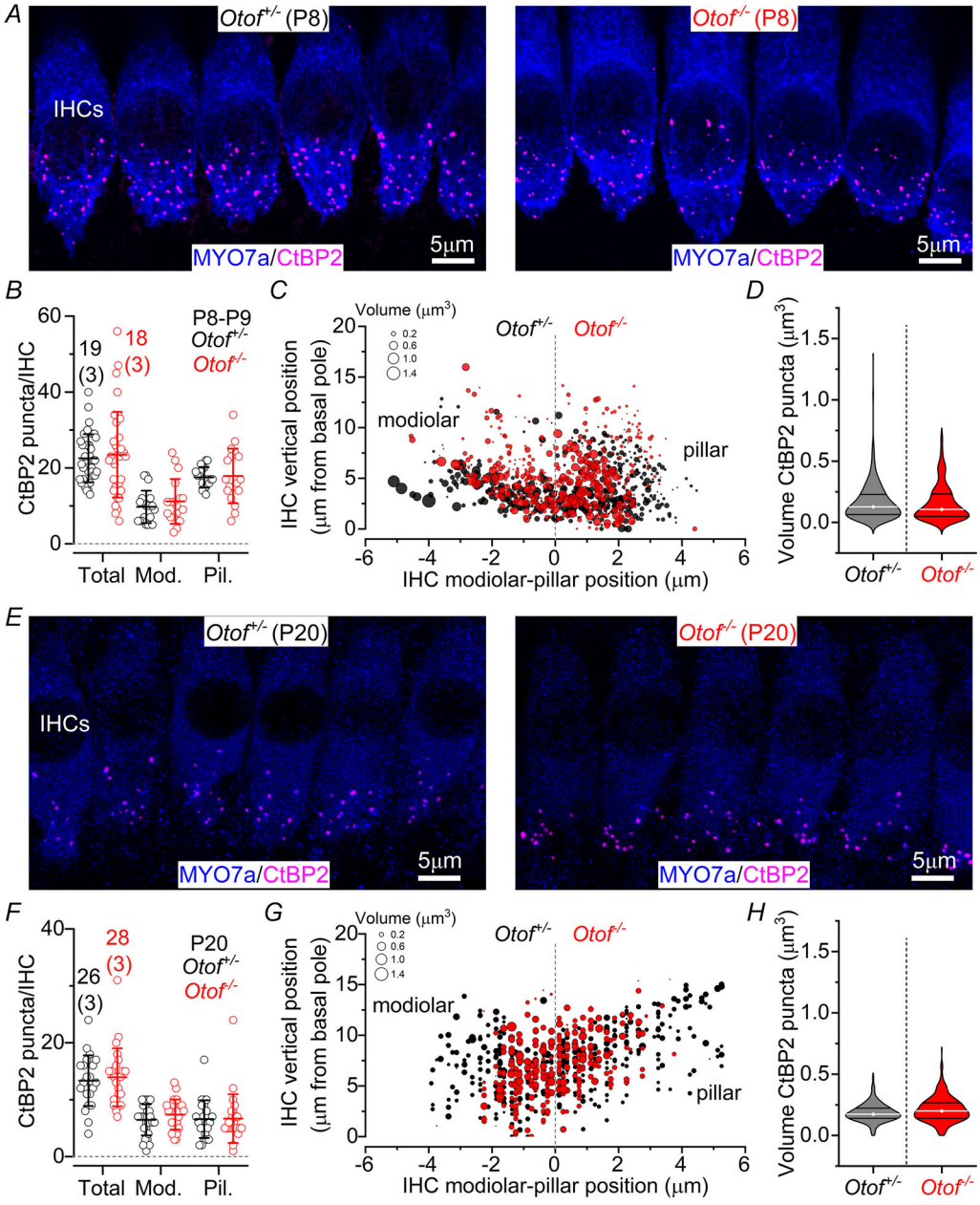

Figure 3. Maturational changes in ribbon synapse between *Otof*$^{+/-}$ and *Otof*$^{-/-}$ mice
A, example of fluorescence micrographs showing the IHCs immunostained for Myo7a (blue) and CtBP2 (hair cell pre-synaptic ribbon marker, magenta) at P8. *B*, total number of pre-synaptic CtBP2 puncta per IHC (left) and that present in the modiolar (Mod., middle) and pillar (Pil., right) IHC regions from control and *Otof*$^{-/-}$ P8–P9 mice (total, $P = 0.9663$; modiolar, $P > 0.9999$; pillar, $P = 0.9876$, Tukey's post-hoc test, one-way ANOVA). *C*, bubble plots representing the distribution along the modiolar-to-pillar (horizontal) and cuticular-to-synaptic (vertical) direction of CtBP2 puncta (total puncta: *Otof*$^{+/-}$ 518; *Otof*$^{-/-}$ 523). The marker size is proportional to the spot volume. *D*, volume of synapses in the IHCs of control and *Otof*$^{-/-}$ P8–P9 mice ($P = 0.0542$; Mann–Whitney test). Data shown in *B–D* were obtained from 19 IHCs from 3 *Otof*$^{+/-}$ mice and 18 IHCs from 3 *Otof*$^{-/-}$ mice. *E*, example of fluorescence micrographs as shown in *A*, but from IHCs of P20 *Otof*$^{+/-}$ and *Otof*$^{-/-}$ mice. *F*, total number of CtBP2 puncta per IHC (left) and that present in the modiolar (Mod.: middle) and pillar (Pil. right) regions in control and *Otof*$^{-/-}$ P20 mice (total, $P = 0.9663$; modiolar, $P = 0.9876$; pillar, $P > 0.9999$). *G*, bubble plots representing the distribution along the modiolar-to-pillar (horizontal) and cuticular-to-synaptic (vertical) direction of CtBP2 puncta (total puncta: *Otof*$^{+/-}$ 375; *Otof*$^{-/-}$ 325). The marker size is proportional to the spot volume. *H*, volume of synapses in the IHCs of control and *Otof*$^{-/-}$ P20 mice ($P = 0.6000$; Mann–Whitney test). Data shown in *F–H* were from the same dataset: 26 IHCs from 3 *Otof*$^{+/-}$ mice and 28 IHCs from 3 *Otof*$^{-/-}$ mice.

using an antibody against b-tubulin, were significantly reduced in *Otof*$^{-/-}$ (500 ± 57 fibres, 3 mice, from 88 µm cochlear distance covering about 9 IHCs) compared to littermate control *Otof*$^{+/-}$ (720 ± 107 fibres, 3 mice, $P = 0.0351$, *t* test) mice. These finding indicate that some of the ribbons in the IHCs of *Otof*$^{-/-}$ mice are not juxtaposed to the post-synaptic terminals, as also suggested by the above transition electron microscopy study (Roux et al., 2006). We also showed that the number of CtBP2 puncta in both *Otof*$^{+/-}$ and *Otof*$^{-/-}$ mice was reduced by about a half between P8 and P20 ($P < 0.0001$ for both genotypes, Tukey's post-hoc test, one-way ANOVA), which also agrees with the expected maturational pruning of synaptic contacts between the SGN terminals and IHCs (e.g. Michanski et al., 2019; Wong et al., 2014). This also indicates that the process of synaptic pruning is independent of otoferlin. We also found that the volume of the CtBP2 puncta and their distribution on the IHC were not changed between *Otof*$^{+/-}$ and *Otof*$^{-/-}$ mice (P8: Fig. 3*C* and *D*; P20: Fig. 3*G* and *H*).

We next investigated whether the biophysical characteristics of the SGNs correlated with the synapse location. As stated above (Fig. 2), the biocytin-containing intracellular solution allowed us to determine the position of the SGN afferent terminals on the IHCs. The location of the afferent synapses on the IHCs was quantified as a normalised basal position (NBP, Fig. 4*A*), indicating how far the synapses are from basal pole (Markowitz & Kalluri, 2020). The measurement of SGN position on an IHC using NBP allowed us to look for any biophysical property that correlated with fibre location and whether this was affected by an absence of otoferlin. In the

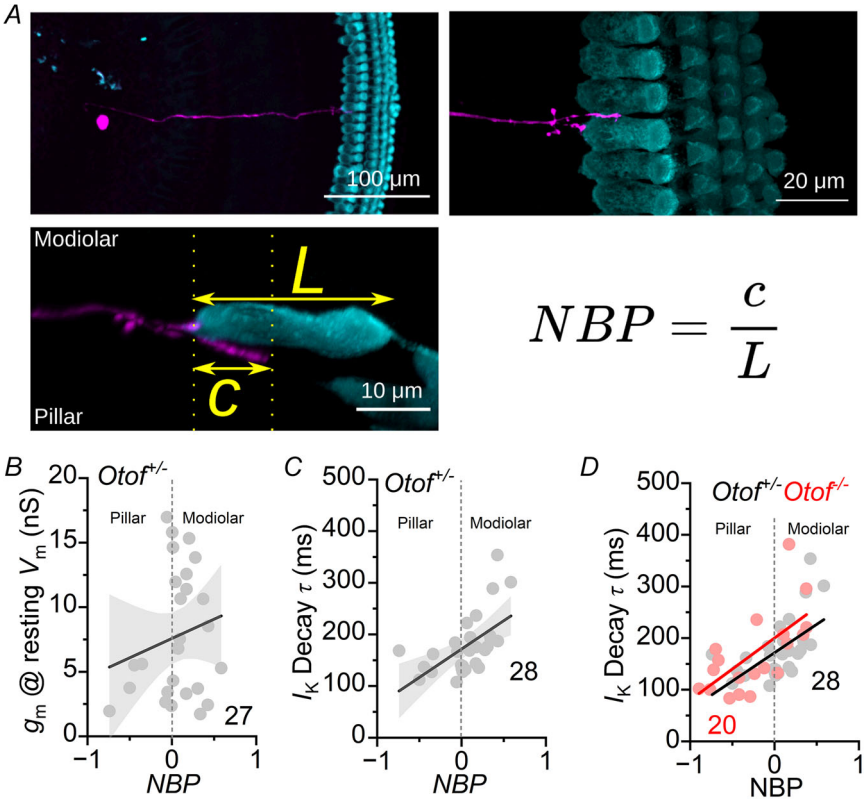

Figure 4. Distribution of SGN afferent terminals around IHCs in *Otof*$^{-/-}$ mice
A, example fluorescence micrographs of the apical coil of the mouse cochlea highlighting the IHCs (turquois) and one SGN filled with biocytin (magenta), at different magnifications (P7, *Otof*$^{+/-}$ mouse). Normalised basal position (NBP) was calculated by dividing the position of the most extreme afferent terminal along the IHC from the base of the cell (*c*) by the total length of the IHC cell (*L*). The NBP values were given a positive value if the SGN contacted the modiolar side of the IHC and a negative value if it contacted the pillar side. *B*, scatter plots showing the variation of resting conductance at the resting membrane potential (g_m at V_m) as a function of their normalised basal position (NBP) around the IHC for single SGNs in *Otof*$^{+/-}$ mice. *C*, decay time constant of the total K^+ current inactivation (I_K decay τ, measured in ms) measured from SGNs in *Otof*$^{+/-}$ mice as a function of NBP. *D*, scatter plots of the decay time constant of the total K^+ current inactivation as in *C* but showing a comparison of values from *Otof*$^{+/-}$ and *Otof*$^{-/-}$ mice. Numbers of SGN investigated are shown on the bottom of *B*–*D*. Number of mice: 25 (*Otof*$^{+/-}$, *B*), 26 (*Otof*$^{+/-}$, *C*), 26 (*Otof*$^{+/-}$, *D*); 19 (*Otof*$^{-/-}$, *D*).

Otof$^{+/-}$ mice, we found that the SGN resting membrane conductance (g_m) did not vary significantly with NBP ($P = 0.4815$, linear model, Fig. 4*B*). The decay time constant of the inactivating component of I_K did vary significantly according to the NBP ($P = 0.0024$, Fig. 4*C*). When the values were separated according to genotype, the trend remained consistent for SGNs from *Otof*$^{+/-}$ and *Otof*$^{-/-}$ mice (Fig. 4*D*).

The progression of potassium and HCN current development is delayed in *Otof*$^{-/-}$ SGNs

The difference in the AP firing profile of SGNs from control *Otof*$^{+/-}$ and *Otof*$^{-/-}$ mice is likely to be correlated with the underlying voltage-gated ion channels present in these neurons. Therefore, we investigated the characteristics of the main voltage-gated membrane currents expressed in SGNs. A typical example of inward and outward currents recorded in response to hyperpolarising and depolarising voltage steps, from a holding potential of −80 mV, is shown Fig. 5*A*. From these recordings, it was possible to identify three main current components: a delayed activating inward current at hyperpolarised potentials (I_H: highlighted in blue in Fig. 5*A*), known to be carried by HCN channels (Kim & Holt, 2013); an initial transient inward current activated at depolarised potentials, which is a combination of inward Ca^{2+} and Na^+ currents that we define as I_{inw} (highlighted in magenta in Fig. 5*A*); and an outward K^+ current that is largely sustained for voltages up to +10 mV and then starts to inactivate at more depolarised potentials (orange symbols and fitting in Fig. 5*A*). In order to quantify these different current components for each SGN, we measured the size of the steady-state I_H at −120 mV, the peak I_{inw} at −20 mV, the sustained outward K^+ current at −40 mV (a potential where there was little current inactivation), and the inactivating K^+ current at 0 mV (measured as the peak minus the steady-state current) (Fig. 5*B*). Although the magnitudes of these SGN current components, apart from I_{inw}, increased during development in mice from both genotypes, the rate of change was significantly lower in *Otof*$^{-/-}$ compared to *Otof*$^{+/-}$ mice (Fig. 5*B*). The age-dependent increase in the magnitudes of the peak and steady-state outward I_K for both *Otof*$^{-/-}$ and *Otof*$^{+/-}$ SGNs was also evident from the overall current–voltage (*I*–*V*) relations for three different age ranges (Fig. 5*C*). In order to compare the voltage-dependence of the steady-state outward I_K between the two genotypes and at the three different age ranges, we generated conductance–voltage curves (Fig. 5*D*). We found that the slope of the curves (k), but not the half-maximal activation (V_h), was significantly different between the two genotypes (k: $P = 0.0007$; V_h: $P = 0.0796$, linear model: Fig. 5*E* and *F*).

The differences we observed in the size of the SGN outward K^+ currents with both age and genotype could be an important factor in determining the mode of AP firing (single, phasic or tonic). To investigate this further, we grouped the SGNs from *Otof*$^{+/-}$ and *Otof*$^{-/-}$ mice according to their AP firing profile and compared the size of the outward K^+ currents between −60 and −30 mV, the physiological range for action potential generation (Fig. 6*A* and *B*). We found that SGNs with larger K^+ currents tended to show the single or phasic AP firing profile, whereas those with the smallest K^+ currents tended to fire tonically. At P6–P8, while *Otof*$^{+/-}$ SGNs were either single firing or phasic (Fig. 6*A*), *Otof*$^{-/-}$ SGNs retained a high proportion of tonic fibres (Fig. 6*B*). In order to identify other SGN biophysical properties that varied according to the mode of AP firing, we pooled the data from both *Otof*$^{+/-}$ and *Otof*$^{-/-}$ mice and correlated each parameter with the neurons firing profile (Fig. 6*C* and *D*). Both the inward Na^+ and Ca^{2+} current size (I_{inw}) and the AP peak amplitude were larger in tonically active neurons compared to single firing (Fig. 6*C*). SGNs showing single or phasic firing had a higher threshold current required to elicit spiking activity (Fig. 6*C*). Finally, the size of the sustained outward K^+ current and its voltage dependence measured from the conductance curves were correlated with the mode of AP firing (Fig. 6*D*), likely reflecting the differences we observed between the *Otof*$^{+/-}$ and *Otof*$^{-/-}$ genotypes (Fig. 5).

The K^+ current composition in SGNs is not affected in *Otof*$^{-/-}$ mice

SGNs express many K^+ channel subtypes (Chen & Davis, 2006; Petitpré et al., 2018; Shrestha et al., 2018; Sun et al., 2018), which can be identified using a cumulative application of selective channel blockers (Johnston et al., 2010). We used this procedure to investigate whether the smaller outward K^+ currents in *Otof*$^{-/-}$ SGNs were due to an absence of a specific K^+ channel type. The total membrane current in SGNs from both *Otof*$^{+/-}$ and *Otof*$^{-/-}$ P5–P6 mice was elicited by applying voltage steps between −60 mV and +20 mV in 20 mV nominal increments. Following the recording of the total current (Fig. 7*A*), the different channel blockers were added to the extracellular solution and applied sequentially to the SGNs using a topical perfusion system (Fig. 7*B*). The current carried by the different channels expressed in the SGNs was obtained by subtracting the current in the presence of the blocker(s) from that of the preceding recording. Examples of the different isolated currents are shown in Fig. 7*C*. TTX blocked a transient and a persistent Na^+ current present in SGNs (Browne et al., 2017). However, we did not observe large TTX sensitive outward currents

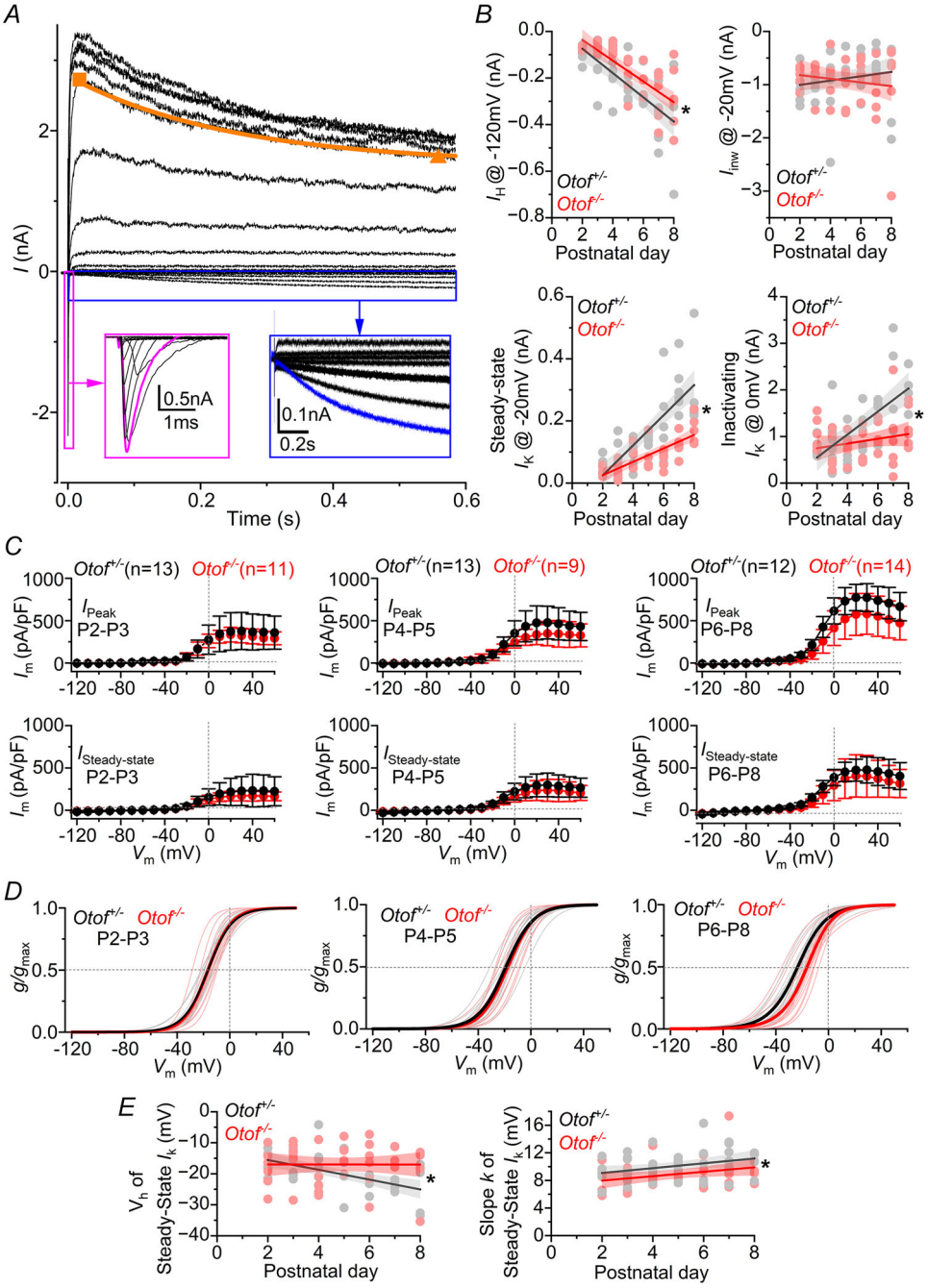

Figure 5. Developmental changes in K+ current expression in SGNs from *Otof*$^{-/-}$ mice
A, example current recording from an SGN of a control *Otof*$^{+/-}$ mouse at P5. Inward and outward currents were obtained by applying voltage steps from −120 mV to +60 mV in 10 mV nominal increments, from the holding potential of −80 mV. The magenta and blue shaded areas and insets highlight the combined inward Ca^{2+} and Na^{+} currents (magenta) and the hyperpolarisation-activated I_H (blue). The inactivation of I_K at depolarised potentials is indicated by the exponential fit (orange) between the peak and steady-state levels. *B*, size of different current components plotted as a function of postnatal age. I_H was measured at −120 mV and at the end of the voltage step (600 ms, blue inset in *A*). The peak I_{inw} was measured at −20 mV (magenta inset in *A*). The sustained outward current was measured at the end of the voltage step at −40 mV. The inactivating I_K was obtained as difference between peak and steady-state (600 ms) outward current at 0 mV (the difference between the orange symbols in *A*). Single data points represent individual SGN. Data are fit with a linear model and shaded areas represent the standard deviation of the fit parameters. Over the P2–P8 age range, significant changes between *Otof*$^{+/-}$ and *Otof*$^{-/-}$ mice were found for the size of the steady-state ($P < 0.0001$) and inactivating ($P = 0.0009$) K^+ currents and I_H ($P = 0.0023$), but not for I_{inw} ($P = 0.4937$). *C*, size of the total peak (upper panels) and steady-state currents

(lower panels) normalised to the SGN capacitance (pA/pF) plotted as a function of the membrane potential for the three age ranges investigated in both *Otof*$^{+/-}$ and *Otof*$^{-/-}$ mice. The number of SGNs recorded for each genotype is stated at the top of the upper panel and applies to the lower panels in this figure. Number of mice: *Otof*$^{+/-}$ 13 (P2–P3), 10 (P4–P5), 12 (P6–P8); *Otof*$^{-/-}$ 9 (P2–P3), 9 (P4–P5), 13 (P6–P8). *D*, activation curves for the steady-state I_K normalised to maximum conductance, for the same three age groups shown in *C* and from both genotypes. The data from each SGN are fitted with a Boltzmann function (shown as faint dots and lines). Thick line represents the average from each group of recordings (age and genotype). *E* and *F*, half-maximum activation and (V_h) and slope factor (k) of the sustained I_K obtained by the fits described in *D*. Average data are reported as means ± SD in all panels.

previously described in mature cultured SGNs (Reijntjes et al., 2019). DtX, which is a Kv1 specific toxin, blocked the majority of the outward K^+ current at voltages between −60 mV and −40 mV (I_{DtX}), but had less of an effect on the K^+ current at more depolarised potentials. The addition of TEA blocked a large component of the K^+ current present at potentials above −40 mV, consistent with a Kv3 subunit-mediated current (I_{TEA}). Finally, the addition of 4-AP blocked the remaining inactivating component of the K^+ current (I_{4AP} = Kv2 and Kv4). A considerable proportion of the outward current was resistant to block with TEA, 4-AP and DtX (I_{resist}), which activated at membrane potentials positive to −20 mV and did not inactivate. The amplitudes and relative contribution of each of the current components for the sustained I_K at −40 mV and the inactivating I_K at 0 mV present in the SGNs from both *Otof*$^{+/-}$ and *Otof*$^{-/-}$ are shown in Fig. 7*D* and *E*, respectively. The above finding indicates that the different voltage responses in the SGNs between the two genotypes (Fig. 2) are unlikely to be due to the absence of a specific K^+ channel subtype.

We then investigated the voltage dependence of I_K inactivation in SGNs by applying long-lasting pre-conditioning voltage steps to membrane potentials between −120 mV and +50 mV in 10 mV increments from the holding potential of −80 mV. Each pre-conditioning step was immediately followed by a test step to +50 mV. The inactivation curve for I_K was obtained by plotting the steady-state current size measured during the test step against the voltage of the conditioning step (Fig. 8*A*). Normally the inactivation of I_K caused by conditioning step depolarisation would cause the current in the test step to decline giving a sigmoid shaped inactivation curve, which was obtained in modiolar SGNs (Fig. 8*A*). However, pillar SGNs from both *Otof*$^{+/-}$ and *Otof*$^{-/-}$ mice tended to show an additional resurgent current (I_{Kres}) component that appeared as a positive hump in the inactivation curve, peaking for conditioning voltages of around 0 mV (Fig. 8*A*). The size of the resurgent K^+ current was defined as the difference between the inactivation curve vales at −20 mV (before the resurgence) and 0 mV (maximal resurgence). Negative values for I_{Kres} indicate that the SGN did not have a resurgent K^+ current component. We found that the amplitude of I_{Kres} recorded from the SGNs of both *Otof*$^{+/-}$ and *Otof*$^{-/-}$mice negatively correlated with the position of the SGN terminals around the IHCs (NBP, $P = 0.0080$, linear model, Fig. 8*B*). SGNs that contacted the pillar face of the IHC usually showed a resurgent K^+ current, whereas those that contacted the modiolar side did not (Fig. 8*C*, $P = 0.0101$, one-way ANOVA). From the pillar SGNs that exhibited I_{Kres} we found that its size was not significantly different between *Otof*$^{+/-}$ (99 ± 77 pF/pA, $n = 4$) and *Otof*$^{-/-}$ (69 ± 79 pF/pA, $n = 8$, $P = 0.05458$) mice.

The global transcriptome of *Otof*$^{-/-}$ modiolus tissue shows a loss of potassium channel expression and altered cholesterol metabolism

To further assess the molecular determinants responsible for the delay in the biophysical developmental of the SGNs in *Otof*$^{-/-}$ mice, we performed RNA-sequencing on the cochlear modiolar tissue (i.e. SGN cell bodies) from *Otof*$^{+/-}$ and *Otof*$^{-/-}$ mice at the pre-hearing age P7, where we had already seen the maturation delay. We began by validating that *Otof* transcript counts were significantly decreased in the *Otof*$^{-/-}$ mice (Fig. 9*A*), although low levels of basal transcripts were seen in the knockouts, which is consistent with previous findings (Roux et al., 2006). Principal component analysis (PCA) of the top 2000 most variable transcripts in each sample showed that PC1, which explained 50% of the variance in the data, captured differences in genotype, with some noise also present from the dissection date (Fig. 9*B*). We next performed different expression analysis between the two different genotypes (Fig. 9*C*) and observed 72 upregulated and 271 downregulated genes. Pathway analysis showed a clear enrichment for neuronal development, voltage gated potassium channels and cholesterol synthesis among the downregulated genes (Fig. 9*D*), as we would expect from the *Otof*$^{-/-}$ phenotype, and validated the measured delay in the maturation of the potassium current. Among the upregulated genes we observed an enrichment for extracellular matrix organisation (Fig. 9*E*). We noted that a wide number of potassium channels were altered, perhaps explaining why the chosen drugs did not have a differential effect (Fig. 9*F*). We used an RNA-scope *in situ* hybridisation approach to validate the expression of *Kcnip3* in the inner ear, which was identified in the RNA sequencing analysis (Fig. 9). Although the focus

of this work is on SGNs, the cryosection used for the staining also contained the vestibular ganglion neuron (VGN) (Fig. 10*A* and *B*). As positive control we have used *Cacna1a*, which was previously identified as a SGN specific gene (Grandi et al., 2020). We found that both *Cacna1a* and *Kcnip3* expression co-localise in some SGNs (Fig. 10*C*). The fluorescence intensity quantification from the SGN expressing *Kcnip3* shows a significant reduction in the expression level in *Otof*$^{-/-}$ compared to littermate *Otof*$^{+/-}$ mice ($P = 0.0006$, Fig. 10*C*).

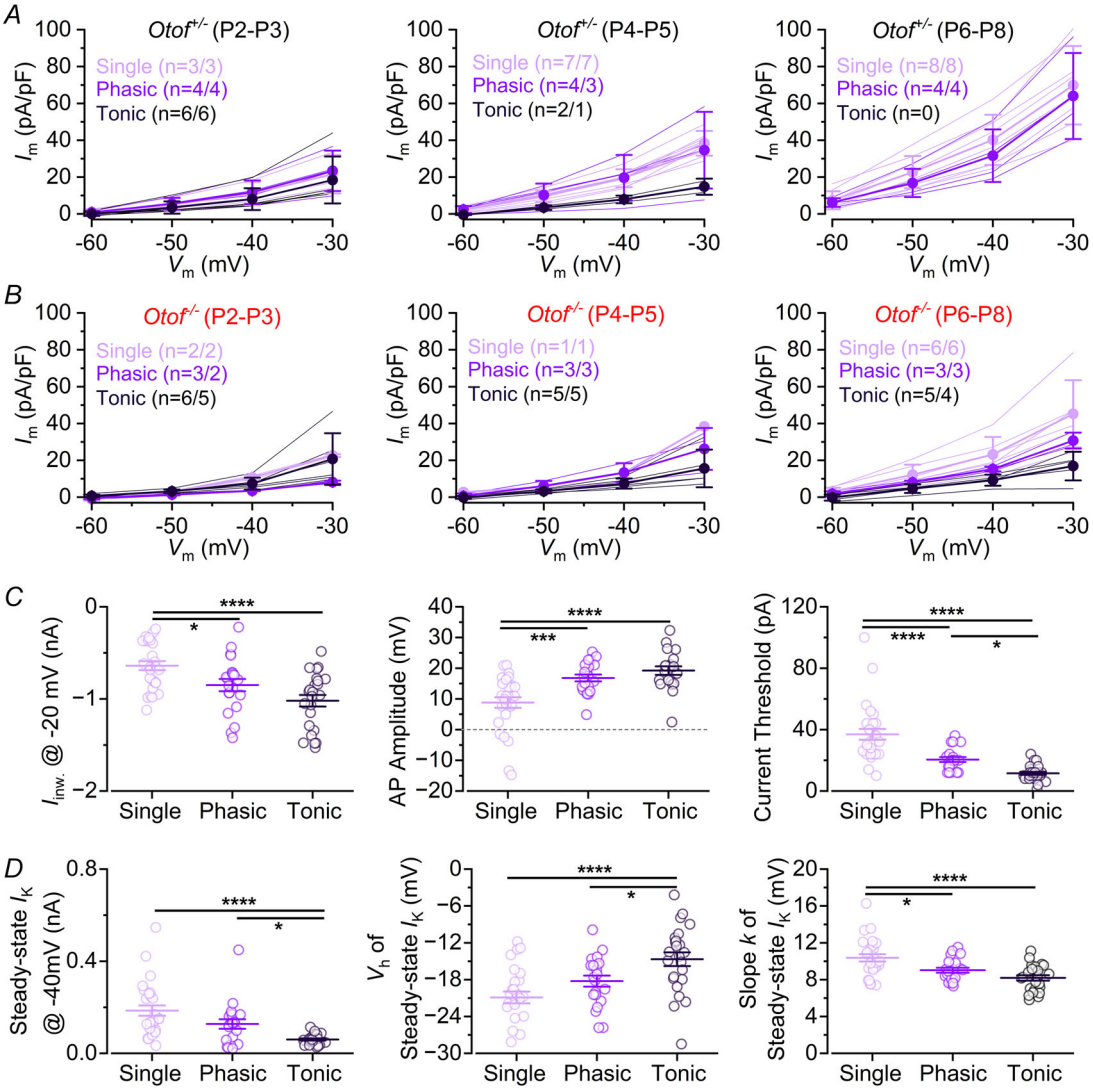

Figure 6. The biophysical characteristics of SGNs is linked to their AP firing profile
A and *B*, outward K^+ current–voltage curves normalised to the SGN capacitance for both *Otof*$^{+/-}$ (*A*) and *Otof*$^{-/-}$ (*B*) at different age ranges. The average curves are grouped, and colour coded, according to the SGN mode of AP firing (single, phasic or tonic). Data from single SGNs are shown as light-coloured lines, below the averages that are the darker lines and filled symbols with SD. *C*, size of I_{inw} measured at −20 mV (left), maximum V_m reached by the first action potential (AP) during depolarising current injection (middle: membrane oscillation smaller than −20 mV were not included) and current injection threshold required to elicit APs in SGNs (right) recorded from SGNs with the three different firing characteristics (single, phasic and tonic). *D*, size of the steady-state or sustained I_K (left), and the V_h (middle) and k (right) obtained from the normalised g_K activation curves in the SGNs grouped according to their firing characteristics. Mean values are shown as horizontal lines, with SD error bars above and below, and single SGN data points as open symbols. Data from *Otof*$^{+/-}$ and *Otof*$^{-/-}$ mice were pooled for these comparisons. Pairwise differences of means between all SGNs with different firing types were tested with Tukey's post-hoc test from one-way ANOVA: $^*P < 0.05$, $^{**}P < 0.01$, $^{***}P < 0.001$, $^{****}P < 0.0001$. In this figure, the number of SGNs and mice used at each genotype and age-range are stated in *A* and *B* in the following format: n = SGNs/mice.

Discussion

The effect of early postnatal inner hair cell (IHC) activity on the maturation of spiral ganglion neuron (SGN) properties remains poorly understood. In this study, we have investigated the biophysical and molecular properties of SGNs during the first postnatal week in the absence of otoferlin (*Otof*), which is the Ca^{2+} sensor required for exocytosis at IHC ribbon synapses. We found that IHC exocytosis is already dependent on otoferlin at postnatal day 1 (P1), which is earlier than previously reported (Beurg et al., 2010). By performing whole-cell recordings from SGNs across ages and genotypes, we found that the absence of *Otof* delays the normal maturation of the SGNs' biophysical

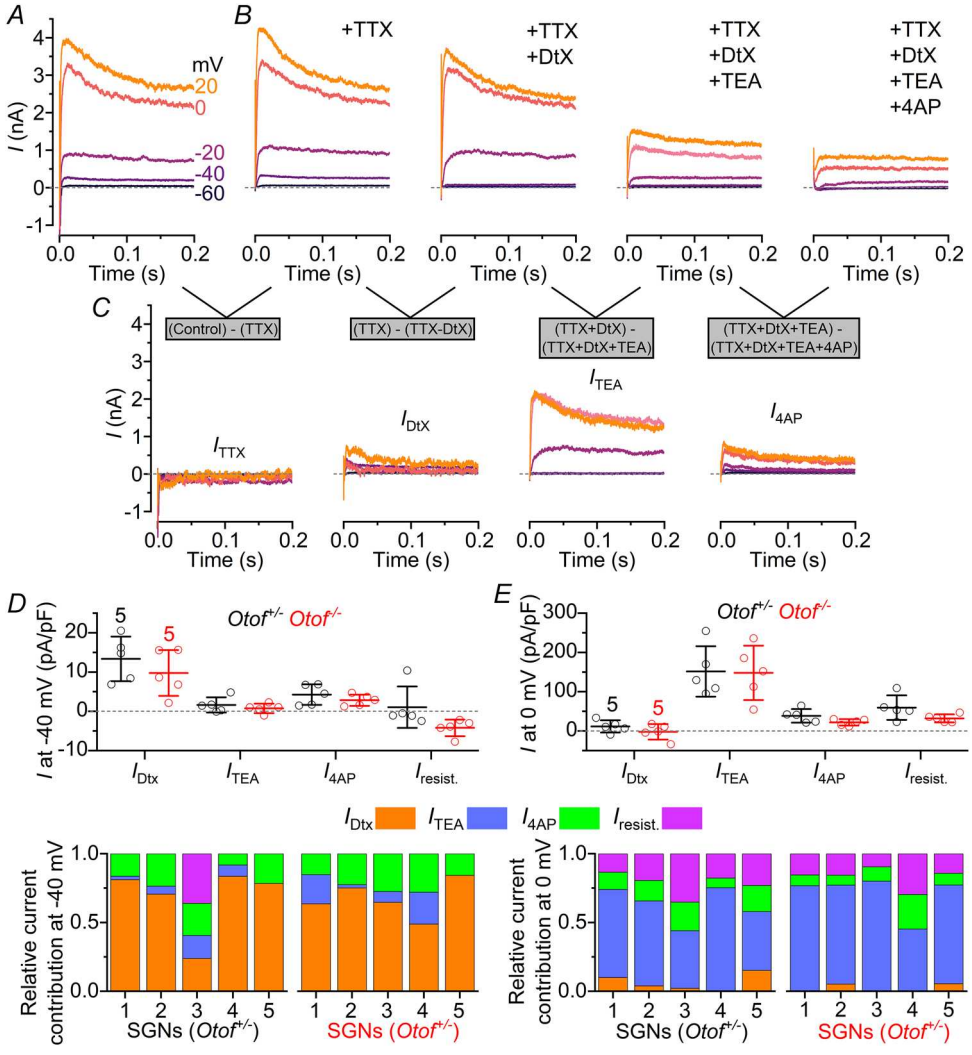

Figure 7. Potassium current profile in SGNs
A, example current recordings from a SGN in a control P5 *Otof*$^{+/-}$ mouse using normal extracellular solution. Currents were elicited by applying voltage steps between −60 mV and +20 mV in 20 mV nominal increments. The traces are colour coded according to voltage. *B*, example currents obtained as described in *A*, from the same SGN, but during the cumulative application of selective channel blockers: TTX (1 µM) blocks the Na^+ channels, DtX (100 nM) blocks K_{v1} subunit-containing K^+-channels, TEA (1 mM) blocks K_v3 channels when already in the presence of DtX, 4-AP (5 mM) blocks K_v2 and K_v4 channels. *C*, isolated currents obtained by subtracting the current traces in the presence of a blocker from the current traces of the preceding application step, i.e. I_{TTX} was obtained by subtracting the current in the presence of TTX from the currents in *A*. I_{DTX} was obtained by subtracting the current in the presence of both TTX and DtX from the current in the presence of TTX, and so on. *D* and *E*, average steady-state current sizes (top panels) and relative contribution of the different current components (bottom panels: 5 SGNs/mice per genotype) isolated by the application of the different channel blockers and measured at −40 mV (*D*) and 0 mV (*E*) in SGNs from *Otof*$^{+/-}$ and *Otof*$^{-/-}$ mice. No statistically significant difference was found in the size of any of the currents between the two genotypes (adjusted *P*-values: I_{DtX} $P = 0.2785$, I_{TEA} $P = 0.7147$, I_{4AP} $P = 0.7147$, I_{resist} $P = 0.1363$).

properties, including their firing patterns and excitability. We showed that SGNs from *Otof*$^{-/-}$ mice failed to up-regulate low-voltage-activated K^+ currents and hyperpolarisation-activated cyclic-nucleotide-gated (HCN) ion channels. The RNA-sequencing data showed downregulation of voltage-gated K^+ channels in *Otof*$^{-/-}$ mice, although the pharmacological experiments did not identify any reduction in a specific sub-class of channels being affected by the lack of otoferlin in the IHCs. Finally, we found that type I SGNs forming axo-somatic terminals with the pillar side of the IHCs selectively expressed a resurgent K^+ current.

Lack of IHC exocytosis delays the maturation of the spiral ganglion neurons

Using *ex vivo* preparations, we found that the biophysical properties of SGNs were consistent with those previously described using cochlear cultures or explants (Crozier & Davis, 2014; Markowitz & Kalluri, 2020). In otoferlin-deficient mice (*Otof*$^{-/-}$), we showed that several biophysical characteristics of the SGNs are down-regulated, resulting in a striking change in their firing pattern. The reduction in input resistance and hyperpolarisation of the resting membrane potential during the first week of development resulted in concomitant changes to latency and threshold of SGN action potential firing in *Otof*-deficient mice. These crucial parameters are controlled by the activity of K_v1 and HCN channels (Liu et al., 2014). Interestingly, the reduction in the size of the of K^+ current in the SGNs of *Otof*$^{-/-}$ mice could not be attributed to down-regulation of a specific type of K^+ channel subunit, indicating that a program of development involving multiple ion channel genes is affected in the *Otof*$^{-/-}$ mice. This is also supported by our RNA-sequencing results suggesting the differential expression of many ion channels, predominantly those for K^+.

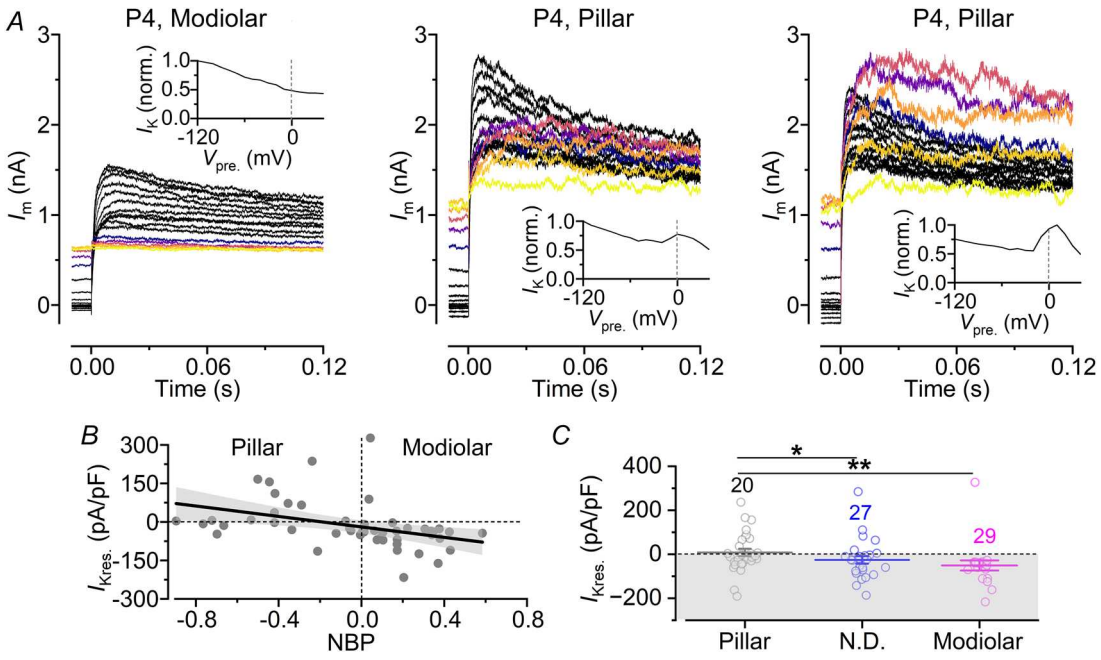

Figure 8. I_K inactivation and a resurgent K^+ current are biophysical markers of SGN sub-population identity
A, example currents recorded from SGNs in a P4 *Otof*$^{+/-}$ mouse whose afferent terminal contacted either the modiolar (left) or pillar (middle and right) side of IHCs. The currents were elicited by a +50 mV voltage step following pre-conditioning steps (V_{pre}) from −120 to +40 mV. The size of the outward current in modiolar SGNs declined with increasing pre-conditioning step membrane potentials (inset, left panel), whereas in several pillar SGNs there was a resurgent current that activated following pre-conditioning pulses of −20 mV to 20 mV (insets, middle and right panels). Traces with pre-conditioning voltages from −10 mV to +40 mV are colour coded. *B*, scatter plot showing the size of I_{Kres} as a function of the position of the SGN afferent terminals around the IHCs (NBP). The fit is from the linear model. *C*, size of I_{Kres} in SGN afferent terminals identified as pillar or modiolar, as well as those whose position was not determined. SGNs that did not express I_{Kres} are within the grey area, i.e. have a negative value for I_{Kres}. Six percent of the SGNs with modiolar terminals and 65% with pillar terminals expressed I_{Kres}. Data shown as means and 95% CI calculated from ANOVA. *B* and *C* include data from both *Otof*$^{+/-}$ (n = 32) and *Otof*$^{-/-}$ (n = 35) mice. The number of SGNs recorded is listed in *C*.

Comparison with another IHC loss of function model

Among the downregulated genes encoding K^+ channels we have identified, *Kncip3* (Calsenillin) is responsible for producing a protein that acts as a calcium transcriptional regulator. In response to changes in intracellular calcium, *Kncip3* expression is able to modulate ion channels and receptors, and therefore neuronal excitability (Lyons & West, 2011). Expression of *Kncip3* was also shown to be reduced in the SGNs of the *VGlut3*$^{-/-}$ mutant mouse (Shrestha et al., 2018), which are characterised, similar to the *Otof*$^{-/-}$ mutants, by a lack of glutamate release by IHCs. Collectively, these findings suggest that molecular maturation of SGNs is reliant on IHC secretion mechanisms (vesicle loading and Ca^{2+} channel coupling). Thus, we hypothesise that the downstream effects of *Otof*$^{-/-}$ and *Vglut3*$^{-/-}$ should cause at least partially overlapping physiological and molecular phenotypes due to the insufficient activation of a pathway critically dependent on Ca^{2+} entry through NMDA receptors (Zhang-Hooks et al., 2016). However, as the RNA-sequencing data from *Vglut3*$^{-/-}$ mice were performed in adult animals (Shrestha et al., 2018), we were not able to compare them to our pre-hearing RNA-sequencing. The failure of SGNs to develop hallmarks of a mature biophysical characteristic (high threshold firing) results in their hyperexcitability, which has been previously interpreted as part of a homeostatic compensation mechanism that serves to maintain SGN firing rate in the absence of IHC input (Babola et al., 2018). However, as our data show, this hyperexcitable phenotype is similar to that of SGNs of newborn mice, and therefore we propose an alternative hypothesis whereby the hyperexcitability observed here is due to a loss of maturation rather than a compensatory change.

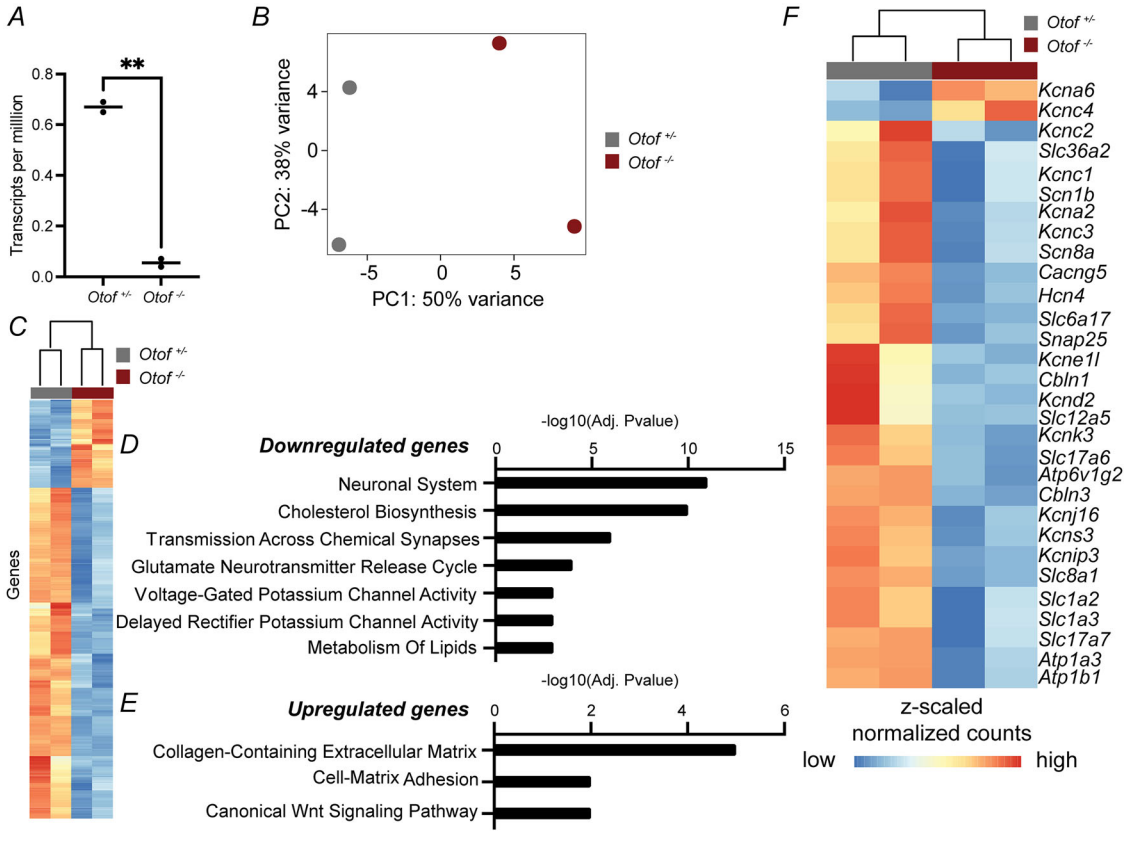

Figure 9. Loss of *Otof* causes transcriptional downregulation of potassium channels
A, transcripts per million of *Otof* in *Otof*$^{+/-}$ and *Otof*$^{-/-}$ cochlear tissue from RNA-sequencing data. *B*, PCA analysis of each RNA-sequencing library; each point represents one library, coloured according to genotype. PC1, which captures 50% of the variance, captures the difference between the genotypes. *C*, heatmap of the normalised counts for all differentially expressed genes (DEGs) as calculated by DESeq2. *D*, pathways associated with downregulated genes from differential expression analysis. *E*, pathways associated with upregulated genes from differential expression analysis. *F*, heatmap of normalised counts for the differentially expressed potassium, sodium and calcium channels and other potassium sensitive proteins.

Biophysical markers for SGN identity

The firing threshold and activity rate of adult SGNs have been shown to correlate with the position of the nerve terminal on the IHC, such that modular fibres had high threshold and low spontaneous rate and pillar fibres had low threshold and high spontaneous rate (cat: Liberman, 1978; mouse: Siebald et al., 2023). Whilst we found that the input resistance and other gross physiological properties of SGNs did not correlate with the position of the nerve terminal on the IHC, we did find that subtle differences in parameters related to K^+ channel inactivation did

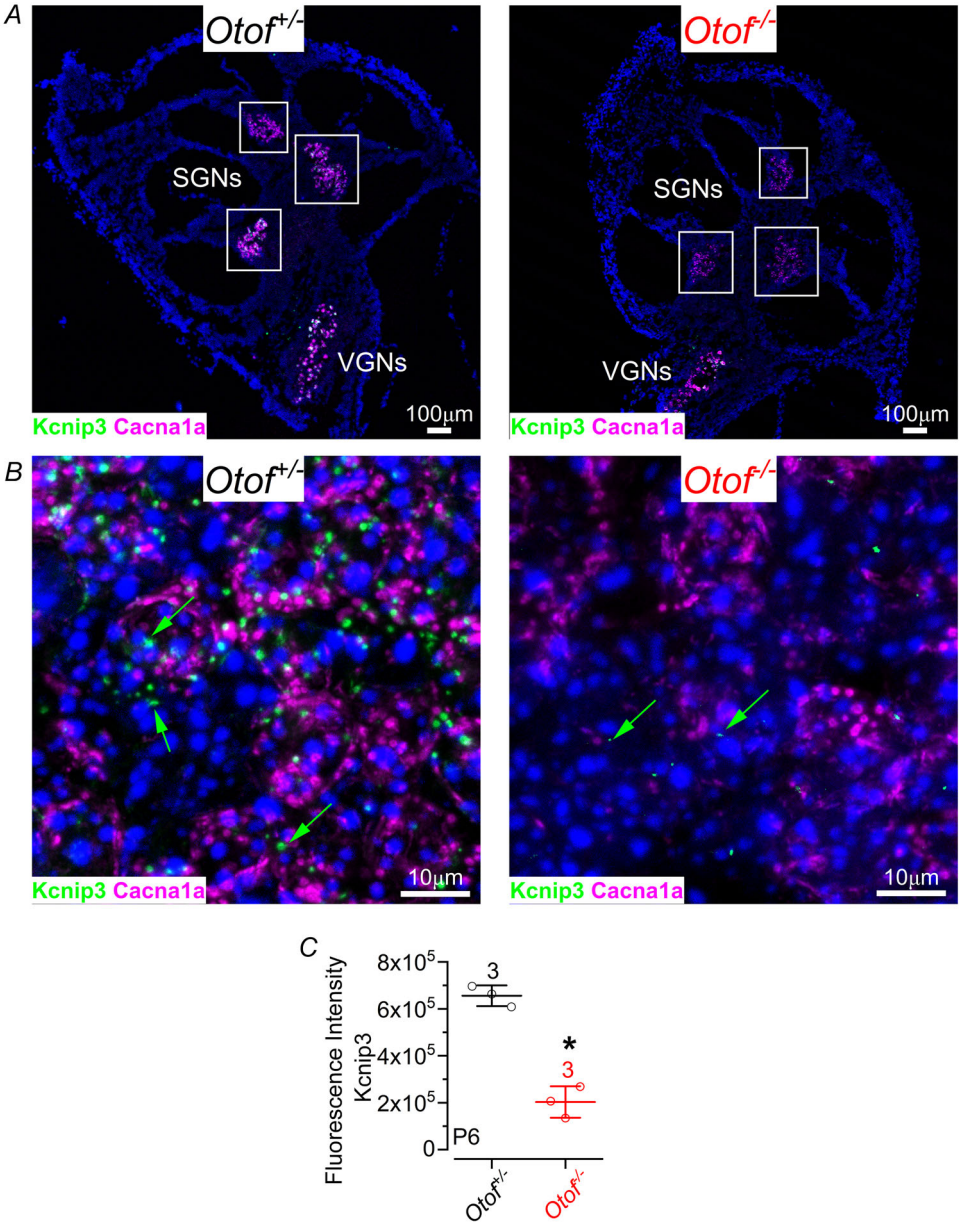

Figure 10. Expression of *Kcnip3* and *Cacna1a* in the cochlea using RNA-scope
A, representative image from RNAscope *in situ* hybridisations of *Cacna1a* (red) and *Kcnip3* (green) from frozen sections of the cochlea and vestibular systems of P6 $Otof^{+/-}$ and $Otof^{-/-}$ mice. White boxes indicate spiral ganglion neurons (SGNs). Both SGNs and vestibular ganglion neurons (VGNs) expressed *Kcnip3* (green) and *Cacna1a* (magenta). *B*, higher resolution images from *A* from the cochlea regions. Green arrows indicate a cell expressing *Kcnip3* while magenta arrows indicate a cell expressing *Cacna1a*. *C*, green fluorescence intensity for *Kcnip3* expression quantified by measuring the raw integrated density of the projected images between $Otof^{+/-}$ and $Otof^{-/-}$ mice ($P = 0.0006$, unpaired two-tailed *t* test). Experiments are from 3 mice.

scale with terminal position on the IHC, such as the current decay time constant value and presence of a resurgent K^+ current. To our knowledge, there are only two potassium channel subunits known that are able to produce resurgent K^+ currents, $K_v3.1$ (Labro et al., 2015) and K_v11 subunits (ERG) (Sanchez-Conde et al., 2022), both of which are expressed in SGNs. The mechanism of resurgence in these channels, however, is different. Resurgence of K_v11 current occurs after completion of an inactivation process (steady-state) (Smith et al., 1996), whereas K_v3 resurgence only becomes apparent after very rapid (1–2 ms) depolarisations resulting in partial activation (Labro et al., 2015). On this basis, the phenomenon observed here is more similar to K_v11 gating. The K_v3 heteromer is composed of $K_v3.1$ (*Kcnc1*), $K_v3.2$ (*Kcnc2*) and $K_v3.3$ (*Kcnc3*). *Kcnc1* and *Kcnc3* are expressed by all three transcriptionally distinct SGN subtypes; however, *Kcnc2* expression is exclusively found in one of the three subtypes (Shrestha et al., 2018). With the complicated assembly of heteromeric K_v3 complexes as well as accessory subunits (Kaczmarek & Zhang, 2017), although very unlikely, we cannot rule out that a K_v3 channel complex specific to SGN subtype underlies the observed differences in the resurgent K^+ currents despite being different from the previously reported K_v3 resurgence characteristics (Labro et al., 2015). From our pharmacology experiments, K_v3 subunit containing, TEA-sensitive channels conduct more than half of the high-voltage-activated outward current. Thus, we hypothesise that changes to K_v3 gene expression between SGN subtypes most likely accounts for the observed differences in K^+ current inactivation parameters between neurons with different synapse positioning.

Collectively, these data suggest that otoferlin-mediated exocytosis is necessary for early development and maturation of SGNs and the K^+ and HCN currents. At early time points (P2–P7), despite the number of synapses being conserved between control and *Otof*$^{-/-}$ animals, the physiological and molecular properties of these neurons are not the same, confirming the important role of early IHC exocytosis in shaping the SGN properties. Although we were not able to determine a specific family of channels regulated by *Otof*, RNA-sequencing revealed a broad set of potassium and sodium channels that were differentially expressed between the two genotypes, among them the Kv3 family that is known to be responsible for resurgent K^+ currents. We hypothesise that the discrepancy of these two findings might be due to the complex compensation mechanism of ion channels, where each channel's expression only changes slightly. Additionally, the RNA-sequencing data showed altered lipid and cholesterol metabolism, which may suggest altered lipid membrane dynamics. However, further work is necessary to understand the role of otoferlin and/or exocytosis in the regulation of membrane dynamics.

References

Adamson, C. L., Reid, M. A., Mo, Z. L., Bowne-English, J., & Davis, R. L. (2002). Firing features and potassium channel content of murine spiral ganglion neurons vary with cochlear location. *Journal of Comparative Neurology*, **447**(4), 331–50.

Al-Moyed, H., Cepeda, A. P., Jung, S., Moser, T., Kügler, S., & Reisinger, E. (2019). A dual-AAV approach restores fast exocytosis and partially rescues auditory function in deaf otoferlin knock-out mice. *European Molecular Biology Organization Molecular Medicine*, **11**(1), e9396.

Babola, T. A., Li, S., Gribizis, A., Lee, B. J., Issa, J. B., Wang, H. C., Crair, M. C., & Bergles, D. E. (2018). Homeostatic control of spontaneous activity in the developing auditory system. *Neuron*, **99**(3), 511–524.

Beurg, M., Michalski, N., Safieddine, S., Bouleau, Y., Schneggenburger, R., Chapman, E. R., Petit, C., & Dulon, D. (2010). Control of exocytosis by synaptotagmins and otoferlin in auditory hair cells. *Journal of Neuroscience*, **30**(40), 13281–13290.

Browne, L., Smith, K. E., & Jagger, D. J. (2017). Identification of persistent and resurgent sodium currents in spiral ganglion neurons cultured from the mouse cochlea. *eNeuro*, **4**(6), 03–17.

Carlton, A. J., Jeng, J. Y., Grandi, F. C., de Faveri, F., Ceriani, F., de Tomasi, L., Underhill, A., Johnson, S. L., Legan, K. P., Kros, C. J., Richardson, G. P., Mustapha, M., & Marcotti, W. (2023). A critical period of prehearing spontaneous Ca^{2+} spiking is required for hair-bundle maintenance in inner hair cells. *European Molecular Biology Organization Journal*, **42**(4), e112118.

Carlton, A. J., Jeng, J. Y., Grandi, F. C., de Faveri, F., Amariutei, A. E., de Tomasi, L., O'Connor, A., Johnson, S. L., Furness, D. N., Brown, S. D. M., Ceriani, F., Bowl, M. R., Mustapha, M., & Marcotti, W. (2024). BAI1 localizes AMPA receptors at the cochlear afferent post-synaptic density and is essential for hearing. *Cell Reports*, **43**(4), 114025.

Chen, W. C., & Davis, R. L. (2006). Voltage-gated and two-pore-domain potassium channels in murine spiral ganglion neurons. *Hearing Research*, **222**(1–2), 89–99.

Crozier, R. A., & Davis, R. L. (2014). Unmasking of spiral ganglion neuron firing dynamics by membrane potential and neurotrophin-3. *Journal of Neuroscience*, **34**(29), 9688–9702.

Davis, R. L., & Crozier, R. A. (2015). Dynamic firing properties of type I spiral ganglion neurons. *Cell and Tissue Research*, **361**(1), 115–127.

Eckrich, T., Blum, K., Milenkovic, I., & Engel, J. (2018). Fast Ca^{2+} transients of inner hair cells arise Coupled and uncoupled to Ca^{2+} waves of inner supporting cells in the developing mouse cochlea. *Frontiers in Molecular Neuroscience*, **11**, 264.

Elzhov, T. V., Mullen, K. M., Spiess, A.-N., & Bolker, B. (2022). minpack.lm: R interface to the levenberg-marquardt nonlinear least-squares algorithm found in MINPACK, plus support for bounds (manual).

Ewels, P. A., Peltzer, A., Fillinger, S., Patel, H., Alneberg, J., Wilm, A., Garcia, M. U., Di Tommaso, P., & Nahnsen, S. (2020). The nf-core framework for community-curated bioinformatics pipelines. *Nature Biotechnology*, **38**, 276–278.

Gillespie, M., Jassal, B., Stephan, R., Milacic, M., Rothfels, K., Senff-Ribeiro, A., Griss, J., Sevilla, C., Matthews, L., Gong, C., Deng, C., Varusai, T., Ragueneau, E., Haider, Y., May, B., Shamovsky, V., Weiser, J., Brunson, T., Sanati, N., … D'Eustachio, P. (2022). The reactome pathway knowledgebase 2022. *Nucleic Acids Research*, **50**, D687–D692.

Grandi, F. C., de Tomasi, L., & Mustapha, M. (2020). Single-cell RNA analysis of type I spiral ganglion neurons reveals a Lmx1a population in the cochlea. *Frontiers in Molecular Neuroscience*, **13**, 83.

Heil, P., & Peterson, A. J. (2015). Basic response properties of auditory nerve fibers: A review. *Cell and Tissue Research*, **361**(1), 129–158.

Johnson, S. L., Ceriani, F., Houston, O., Polishchuk, R., Polishchuk, E., Crispino, G., Zorzi, V., Mammano, F., & Marcotti, W. (2017). Connexin-mediated signaling in non-sensory cells is crucial for the development of sensory inner hair cells in the mouse cochlea. *Journal of Neuroscience*, **37**(2), 258–268.

Jones, T. A., Leake, P. A., Snyder, R. L., Stakhovskaya, O., & Bonham, B. (2007). Spontaneous discharge patterns in cochlear spiral ganglion cells before the onset of hearing in cats. *Journal of Neurophysiology*, **98**(4), 1898–1908.

Johnson, S. L., Eckrich, T., Kuhn, S., Zampini, V., Franz, C., Ranatunga, K. M., Roberts, T. P., Masetto, S., Knipper, M., Kros, C. J., & Marcotti, W. (2011). Position-dependent patterning of spontaneous action potentials in immature cochlear inner hair cells. *Nature Neuroscience*, **14**(6), 711–717.

Johnston, J., Forsythe, I. D., & Kopp-Scheinpflug, C. (2010). Going native: Voltage-gated potassium channels controlling neuronal excitability. *The Journal of Physiology*, **588**(Pt 17), 3187–200.

Kaczmarek, L. K., & Zhang, Y. (2017). Kv3 channels: Enablers of rapid firing, neurotransmitter release, and neuronal endurance. *Physiological Reviews*, **97**(4), 1431–1468.

Kim, Y. H., & Holt, J. R. (2013). Functional contributions of HCN channels in the primary auditory neurons of the mouse inner ear. *Journal of General Physiology*, **142**(3), 207–223.

Labro, A. J., Priest, M. F., Lacroix, J. J., Snyders, D. J., & Bezanilla, F. (2015). Kv3.1 uses a timely resurgent K^+ current to secure action potential repolarization. *Nature Communications*, **6**, 10173.

Lawrence, M., Gentleman, R., & Carey, V. (2009). rtracklayer: an R package for interfacing with genome browsers. *Bioinformatics*, **25**, 1841–1842.

Lawrence, M., Huber, W., Page's, H., Aboyoun, P., Carlson, M., Gentleman, R., Morgan, M. T., & Carey, V. J. (2013). Software for computing and annotating genomic ranges. *PLoS Computational Biology*, **9**, e1003118.

Liberman, M. C. (1978). Auditory-nerve response from cats raised in a low-noise chamber. *Journal of the American Statistical Association*, **63**(2), 442–455.

Liberman, M. C., Dodds, L. W., & Pierce, S. (1990). Afferent and efferent innervation of the cat cochlea: Quantitative analysis with light and electron microscopy. *Journal of Comparative Neurology*, **301**(3), 443–460.

Liu, Q., Manis, P. B., & Davis, R. L. (2014). I h and HCN channels in murine spiral ganglion neurons: Tonotopic variation, local heterogeneity, and kinetic model. *Journal of the Association for Research in Otolaryngology*, **15**(4), 585–599.

Love, M. I., Huber, W., & Anders, S. (2014). Moderated estimation of fold change and dispersion for RNA-seq data with DESeq2. *Genome Biology*, **15**, 550.

Lyons, M. R., & West, A. E. (2011). Mechanisms of specificity in neuronal activity-regulated gene transcription. *Progress in Neurobiology*, **94**(3), 259–295.

Marcotti, W., Johnson, S. L., Holley, M. C., & Kros, C. J. (2003). Developmental changes in the expression of potassium currents of embryonic, neonatal and mature mouse inner hair cells. *The Journal of Physiology*, **548**, 383–400.

Markowitz, A. L., Iyer, M. R., & Kalluri, R. (2022). Patch-clamp recordings and single fiber labeling from spiral ganglion somata in acutely prepared semi-intact cochleae from neonatal rats. *Bio-Protocol*, **12**(1), e4281.

Markowitz, A. L., & Kalluri, R. (2020). Gradients in the biophysical properties of neonatal auditory neurons align with synaptic contact position and the intensity coding map of inner hair cells. *eLife*, **9**, e55378.

McQueen, J. (1967). Some methods for classification and analysis of multivariate observations. *Computer and Chemistry*, **4**, 257–272.

Meyer, A. C., Frank, T., Khimich, D., Hoch, G., Riedel, D., Chapochnikov, N. M., Yarin, Y. M., Harke, B., Hell, S. W., Egner, A., & Moser, T. (2009). Tuning of synapse number, structure and function in the cochlea. *Nature Neuroscience*, **12**(4), 444–453.

Michanski, S., Smaluch, K., Steyer, A. M., Chakrabarti, R., Setz, C., Oestreicher, D., Fischer, C., Möbius, W., Moser, T., Vogl, C., & Wichmann, C. (2019). Mapping developmental maturation of inner hair cell ribbon synapses in the apical mouse cochlea. *Proceedings National Academy of Science USA*, **116**(13), 6415–6424.

Morgan, M., Page's, H., Obenchain, V., & Hayden, N. (2023). Rsamtools: Binary alignment (BAM), FASTA, variant call (BCF), and tabix file import. R package version 2.16.0. h.

Mukamel, E. A., & Ngai, J. (2019). Perspectives on defining cell types in the brain. *Current Opinion in Neurobiology*, **56**, 61–68.

Patro, R., Duggal, G., Love, M., Love, M. I., Irizarry, R. A., & Kingsford, C. (2017). Salmon provides fast and bias-aware quantification of transcript expression. *Nature Methods*, **14**, 417–419.

Petitpré, C., Bourien, J., Wu, H., Diuba, A., Puel, J.-L., & Lallemend, F. (2020). Genetic and functional diversity of primary auditory afferents. *Current Opinion in Physiology*, **18**, 85–94.

Petitpré, C., Faure, L., Uhl, P., Fontanet, P., Filova, I., Pavlinkova, G., Adameyko, I., Hadjab, S., & Lallemend, F. (2022). Single-cell RNA-sequencing analysis of the developing mouse inner ear identifies molecular logic of auditory neuron diversification. *Nature Communications*, **13**, 3878.

Petitpré, C., Wu, H., Sharma, A., Tokarska, A., Fontanet, P., Wang, Y., Helmbacher, F., Yackle, K., Silberberg, G., Hadjab, S., & Lallemend, F. (2018). Neuronal heterogeneity and stereotyped connectivity in the auditory afferent system. *Nature Communications*, **9**(1), 3691.

Prescott, S. A., de Koninck, Y., & Sejnowski, T. J. (2008). Biophysical basis for three distinct dynamical mechanisms of action potential initiation. *PLoS Computational Biology*, **4**(10), e1000198.

Pujol, R., Lavigne-Rebillard, M., & Lenoir, M. (1998). Development of sensory and neural structures in the mammalian cochlea. *Springer Handbook of Auditory Research*, **XII**, 146–192.

Pumo, G. M., Kitazawa, T., & Rijli, F. M. (2022). Epigenetic and transcriptional regulation of spontaneous and sensory activity dependent programs during neuronal circuit development. *Frontiers in Neural Circuits*, **16**, 911023.

Reijntjes, D. O. J., Lee, J. H., Park, S., Schubert, N. M. A., van Tuinen, M., Vijayakumar, S., Jones, T. A., Jones, S. M., Gratton, M. A., Xia, X. M., Yamoah, E. N., & Pyott, S. J. (2019). Sodium-activated potassium channels shape peripheral auditory function and activity of the primary auditory neurons in mice. *Scientific Reports*, **9**, 2573.

Roux, I., Safieddine, S., Nouvian, R., Grati, M., Simmler, M.-C., Bahloul, A., Perfettini, I., Le Gall, M., Rostaing, P., Hamard, G., Triller, A., Avan, P., Moser, T., & Petit, C. (2006). Otoferlin, defective in a human deafness form, is essential for exocytosis at the auditory ribbon synapse. *Cell*, **127**(2), 277–289.

Ryugo, D. K. (1992). The auditory nerve: peripheral innervation, cell body morphology, and central projections. In D. B. Webster, A. N. Popper, & R. R. Fay (Eds), *The Mammalian* Auditory Pathway: Neuroanatomy (pp. 23–65). Springer, New York.

Sanchez-Conde, F. G., Jimenez-Vazquez, E. N., Auerbach, D. S., & Jones, D. K. (2022). The ERG1 K^+ channel and its role in neuronal health and disease. *Frontiers in Molecular Neuroscience*, **15**, 890368.

Sanders, T. R., & Kelley, M. W. (2022). Specification of neuronal subtypes in the spiral ganglion begins prior to birth in the mouse. *Proceedings of the National Academy of Sciences, USA*, **119**(48), e2203935119.

Shrestha, B. R., Chia, C., Wu, L., Kujawa, S. G., Liberman, M. C., & Goodrich, L. V. (2018). Sensory neuron diversity in the inner ear is shaped by activity. *Cell*, **174**(5), 1229–1246.

Siebald, C., Vincent, P. F. Y., Bottom, R. T., Sun, S., Reijntjes, D. O. J., Manca, M., Glowatzki, E., & Müller, U. (2023). Molecular signatures define subtypes of auditory afferents with distinct peripheral projection patterns and physiological properties. *Proceedings of the National Academy of Science, USA*, **120**(31), e2217033120.

Smith, P. L., Baukrowitz, T., & Yellen, G. (1996). The inward rectification mechanism of the HERG cardiac potassium channel. *Nature*, **379**(6568), 833–836.

Sonntag, M., Englitz, B., Kopp-Scheinpflug, C., & Rübsamen, R. (2009). Early postnatal development of spontaneous and acoustically evoked discharge activity of principal cells of the medial nucleus of the trapezoid body: An in vivo study in mice. *Journal of Neuroscience*, **29**(30), 9510–9520.

Stalmann, U., Franke, A. J., Al-Moyed, H., Strenzke, N., & Reisinger, E. (2021). Otoferlin is required for proper synapse maturation and for maintenance of inner and outer hair cells in mouse models for DFNB9. *Frontiers in Cellular Neuroscience*, **15**, 677543.

Sun, S., Babola, T., Pregernig, G., So, K. S., Nguyen, M., Su, S.-S. M., Palermo, A. T., Bergles, D. E., Burns, J. C., & Müller, U. (2018). Hair cell mechanotransduction regulates spontaneous activity and spiral ganglion subtype specification in the auditory system. *Cell*, **174**(5), 1247–1263.

Tertrais, M., Bouleau, Y., Emptoz, A., Belleudy, S., Sutton, R. B., Petit, C., Safieddine, S., & Dulon, D. (2019). Viral transfer of mini-otoferlins partially restores the fast component of exocytosis and uncovers ultrafast endocytosis in auditory hair cells of otoferlin knock-out mice. *Journal of Neuroscience*, **39**(18), 3394–3411.

Tritsch, N. X., Yi, E., Gale, J. E., Glowatzki, E., & Bergles, D. E. (2007). The origin of spontaneous activity in the developing auditory system. *Nature*, **450**(7166), 50–55.

Turrigiano, G. G., & Nelson, S. B. (2004). Homeostatic plasticity in the developing nervous system. *Nature Review Neuroscience*, **5**(2), 97–107.

Vincent, P. F., Bouleau, Y., Charpentier, G., Emptoz, A., Safieddine, S., Petit, C., & Dulon, D. (2017). Different CaV1.3 channel isoforms control distinct components of the synaptic vesicle cycle in auditory inner hair cells. *Journal of Neuroscience*, **37**(11), 2960–2975.

Wang, H. C., Lin, C.-C., Cheung, R., Zhang-Hooks, Y., Agarwal, A., Ellis-Davies, G., Rock, J., & Bergles, D. E. (2015). Spontaneous activity of cochlear hair cells triggered by fluid secretion mechanism in adjacent support cells. *Cell*, **163**(6), 1348–1359.

West, A. E., & Greenberg, M. E. (2011). Neuronal activity-regulated gene transcription in synapse development and cognitive function. *Cold Spring Harbor Perspectives in Biology*, **3**(6), a005744.

Wong, A. B., Rutherford, M. A., Gabrielaitis, M., Pangrsic, T., Göttfert, F., Frank, T., Michanski, S., Hell, S., Wolf, F., Wichmann, C., & Moser, T. (2014). Developmental refinement of hair cell synapses tightens the coupling of Ca^{2+} influx to exocytosis. *European Molecular Biology Organization Journal*, **33**(3), 247–264.

Wickham, H., Averick, M., Bryan, J., Chang, W., McGowan, L. D., François, R., Grolemund, G., Hayes, A., Henry, L., Hester, J., Kuhn, M., Pedersen, T. L., Miller, E., Bache, S. M., Müller, K., Ooms, J., Robinson, D., Seidel, D. P., Spinu, V., … Yutani, H. (2019). Welcome to the Tidyverse. *The Journal of Open Source Software*, **4**(43), 1686.

Winter, I. M., Robertson, D., & Yates, G. K. (1990). Diversity of characteristic frequency rate-intensity functions in guinea pig auditory nerve fibres. *Hearing Research*, **45**(3), 191–202.

Zeng, H., & Sanes, J. R. (2017). Neuronal cell-type classification: Challenges, opportunities and the path forward. *Nature Reviews Neuroscience*, **18**(9), 530–546.

Zhang-Hooks, Y., Agarwal, A., Mishina, M., & Bergles, D. E. (2016). NMDA receptors enhance spontaneous activity and promote neuronal survival in the developing cochlea. *Neuron*, **89**(2), 337–350.

Zhou, Y., Zhou, B., Pache, L., Chang, M., Khodabakhshi, A. H., Tanaseichuk, O., Benner, C., & Chanda, S. K. (2019). Metascape provides a biologist-oriented resource for the analysis of systems-level datasets. *Nature Communications*, **10**, 1523.

Additional information

Data availability statement

The data that support the findings of this study are available from the corresponding author upon reasonable request. RNA-sequencing data have been deposited in GEO under accession number GSE242669.

Competing interests

The authors declare no conflict of interest.

Author contributions

L.J.C. performed the SGN experiments and drafted the manuscript. F.C.G. performed the RNA Sequencing experiments. P.Z. performed the RNA Scope work. J.-Y.J. and A.J.C. performed the immunofluorescence experiments. S.L.J. performed the IHC capacitance measurements. W.M., S.L.J., and M.M. conceived and coordinated the study. All authors approved the final version of the manuscript. All authors agree to be accountable for all aspects of the work in ensuring that questions related to the accuracy or integrity of any part of the work are appropriately investigated and resolved. All persons designated as authors qualify for authorship, and all those who qualify for authorship are listed.

Funding

This work was supported by the MRC (MR/S002510/1) to M.M., BBSRC (BB/S006257/1) to S.L.J. and W.M. (BB/X000567/1) to S.L.J. and M.M. and the RNID and Dunhill Medical Trust Fellowship (PA28) to J.-Y.J.

Acknowledgements

Mice were donated by Saaid Safieddine. The authors also thank Michell Bird and Matthew A. Loczki for his assistance with the mouse colonies and Catherine Gennery and Niovi Voulgari for assistance with genotyping. Confocal images were acquired using the Zeiss LSM 880 Airyscan microscope at the Wolfson Light Microscope Facility.

Keywords

afferent fibres, cochlea, development, inner hair cells, potassium currents, spiral ganglion neurons

Supporting information

Additional supporting information can be found online in the Supporting Information section at the end of the HTML view of the article. Supporting information files available:

Peer Review History